Hierarchical high-throughput screening of alkaline-stable lithium-ion conductors combining machine learning and first-principles calculations

Zhuohan Li •*, 1 KyuJung Jun •*, 2 Bowen Deng •, 2 and Gerbrand Ceder •1, 2, *

¹Materials Sciences Division, Lawrence Berkeley National Laboratory, California 94720, United States

²Department of Materials Science and Engineering,

University of California, Berkeley, California 94720, United States[†]

The advancement of solid-state batteries depends on the development of lithiumion conductors that exhibit both high ionic conductivity and stability across a wide
range of electrochemical and chemical conditions. In this paper, we investigate the
chemical factors that control the stability of Li-NASICONs and garnets in highly
alkaline aqueous environment. While this is of general importance, it is particularly
important for the operation of Li-air cells with humidified air. Humid air promotes
the formation of LiOH as the discharge product, creating a highly alkaline environment on the surface of cathode and solid-state electrolyte. In this work, we combine machine learning and first-principles calculations to conduct a high-throughput
computational screening of alkaline-stable oxide-based Li-ion conductors in order to
better characterize the tradeoff between the various relevant properties. We evaluate
the material stability in terms of pH, voltage, and species present in the environment
(LiOH and H_2O) across a vast range of chemical compositions with NASICON and
garnet crystal structures. We utilize a universal machine learning interatomic po-

tential (uMLIP)—CHGNet model—for pre-screening, followed by density functional theory calculations. Such a hierarchical screening procedure enables the evaluation of over 320,000 chemical compositions, encompassing nearly the entire periodic table. From this set 209 alkaline-stable NASICON and garnet compounds are selected as final candidates. We identify the specific cation substitutions that improve alkaline stability in NASICON and garnet compounds, and reveal the underlying mechanism. We also discover the trade-offs for designing alkaline-stable Li-ion conductors, high-lighting the need to carefully optimize compositions so that it can simultaneously enhance all the material properties required for practical battery applications, including synthesizability, stability during battery operation, and Li-ion and electronic conductivities.

I. INTRODUCTION

Li-ion-based energy storage technologies have emerged as a crucial solution to enable the transition to a net-zero carbon emission society. Despite remarkable advancements in current Li-ion batteries, the ever-growing energy demand necessitates the development of new technologies with improved capacity and cost efficiency. Solid-state batteries, in which the liquid electrolyte is replaced by solid-state electrolyte (SSE), are a promising next-generation system. Various types of SSE with different anion chemistries have been investigated so far, including oxide [1–4], sulfide[5–7], and halide-based[8, 9] materials, each offering distinct advantages and disadvantages. Sulfide SSEs exhibit the highest Li-ion conductivities, but have the narrowest electrochemical stability window[10–12]. Recent developments in halide

 $^{^{*}}$ Correspondence: gceder@berkeley.edu

[†] Z.L and K.J. contributed equally to this work

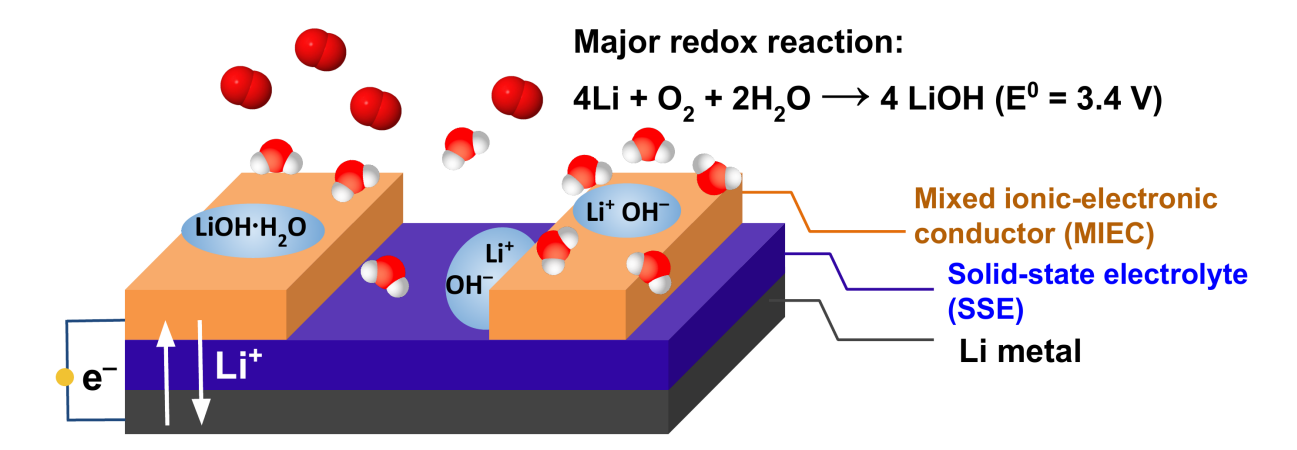


FIG. 1. Schematic illustration of solid-state Li-O_2 battery operated under humid environment

conductors show the high potential of this chemistry as it may combine the high Li-ion conductivity and mechanical flexibility found in sulfides with the good oxidation stability of oxides [8].

Water stability is a common issue among all three types of SSEs. Since water molecules are ubiquitous in the atmosphere, the instability against H₂O poses challenges in the handling and the long-period operation of solid-state batteries. For example, sulfide-based solid electrolytes such as Li₁₀GeP₂S₁₂[6], argyrodite-type Li₆PS₅Cl[5] are less practical due to their spontaneous reaction with H₂O to form H₂S gas [13]. Chloride-based solid electrolytes such as Li₃YCl₆ and Li₃InCl₆ are also found to deteriorate rapidly upon absorption of water[14]. Although the reactivity of oxides with H₂O is much lower, the Li⁺ in the oxides is subject to a topotactic exchange with H⁺ from water [15, 16], which may lead to a reduction of the Li-ion conductivity[17]. Moreover, this Li⁺/H⁺ exchange promotes the formation of LiOH on the surface of the oxide-based conductors [18, 19]. The highly hydrophilic nature of LiOH [20, 21] further facilitates water adsorption and formation of hydrated LiOH droplets [22], creating a highly corrosive alkaline environment. The pH in these droplets can be as high as ~15, determined by the saturation concentration of LiOH in water [21].

The high alkalinity is especially a problem for solid-state Li-O_2 batteries operated with humid air, where LiOH forms as the discharge product as schematically illustrated in Figure 1. In contrast to the current Li-ion batteries, where Li⁺ is inserted into and extracted from the cathode material, Li-O₂ batteries store energy by forming various lithium oxides, such as peroxide, superoxide, and hydroxides, as the discharge product inside the cathode pores. The low mass density of these products makes the Li-O₂ battery concept attractive for its uniquely high specific energy density [23–25]. Conventional Li-O₂ batteries are operated with dry O_2 gas and a liquid electrolyte. Increased humidity facilitates the formation of LiOH as the discharge product, replacing Li₂O₂ that forms under dry condition [26–29]. The change in chemistry has several advantages. First of all, it can increase the discharge voltage from 2.96 V for Li₂O₂ to 3.4 V for LiOH[30]. Second, the formation of LiOH under humid air benefits the discharge capacity as the solution-mediated growth mechanism promotes LiOH growth, in contrast to the insulating and growth-limited Li₂O₂[31–34]. Finally, the higher ionic and electronic conductivity of LiOH also helps reduce the charge overpotential [27, 33, 35]. The potential parasitic reaction between H₂O in the air and the Li metal anode can be mitigated by replacing the liquid electrolyte with a SSE, which physically blocks water molecules from reaching the Li metal anode. In addition, a carbon-free cathode design by using a mixedionic electronic conductor (MIEC) as the porous cathode material can prevent the formation of undesirable Li₂CO₃ during the discharge, effectively reducing the charge overpotential [34].

To operate Li-O₂ batteries under humid conditions, the surfaces of both the SSE and the MIEC cathode must be highly resistant to the highly alkaline and corrosive environment. In this work, we conduct high-throughput computational screening to identify alkaline-stable Li-ion conductors. Our focus is on improving the materials stability against the conditions encountered on the cathode side during battery operation, including high pH

(alkaline stability), applied voltage (electrochemical stability), parasitic chemical reactions with chemical species in the environment (chemical stability). Our strategy is to perform compositional substitution into the NASICON and garnet crystal frameworks as they are known to exhibit high Li-ion conductivity ($\sim 0.1-1 \text{ mS/cm}$)[1, 2]. The crystal structures of NASICON-type and garnet-type Li-ion conductors are depicted in Figure 2(a).

To fully understand the tradeoffs between various properties across chemistry, we aim to explore a chemical space as broadly as possible with the aid of universal machine learning interatomic potential (uMLIP), which significantly accelerates the the evaluation of energies and properties. More specifically, we use the CHGNet MLIP model [36] to perform prescreening over 320,000 different substitutions in NASICON and garnet frameworks. The prescreened subsets of candidates are then further downselected through stability evaluations using density functional theory (DFT) calculations to achieve higher fidelity. Finally, we perform MLIP assisted molecular dynamics (MD) simulations on a subset of final candidate compounds using a fine-tuned CHGNet model to evaluate their Li-ion conductivities. Our hierarchical screening demonstrates a combination of MLIP, and DFT calculations to address materials design challenges.

II. SCREENING METHODOLOGIES

A. Crystal frameworks and substitution chemical space

For NASICON compounds, we adopt the crystal structures with R $\overline{3}$ C symmetry and with the chemical formula $\text{Li}_x(\text{M}_y\text{M}'_{1-y})_2(\text{A}_z\text{A}'_{1-z}\text{O}_4)_3$. The cations A and A' occupy the tetrahedral sites that are coordinated by four oxygen atoms forming the polyanion group, and M and M' occupy octahedral sites that are corner-sharing with the six surrounding tetrahedral

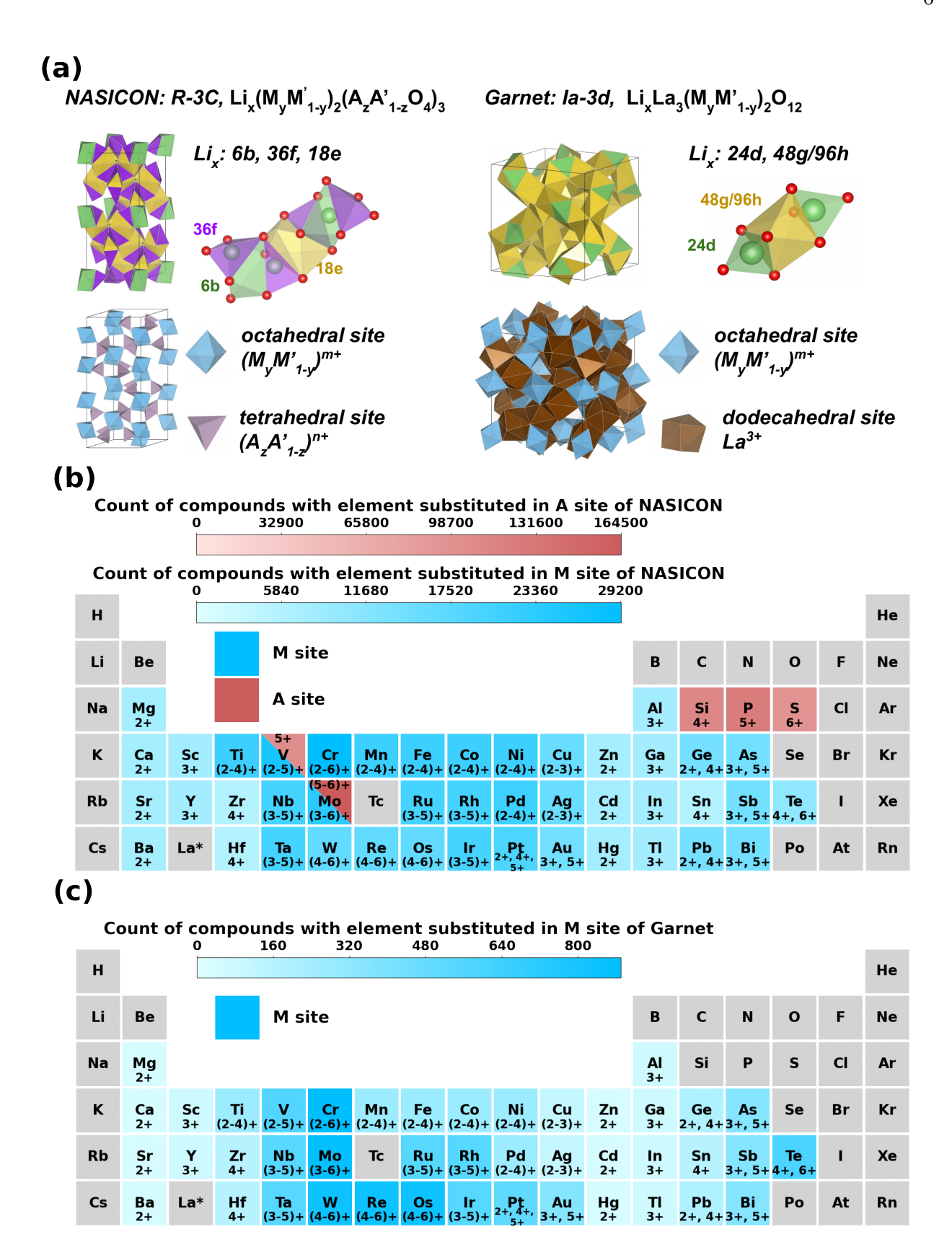


FIG. 2. Crystal frameworks and substitution chemical space for screening (a) Crystal frameworks and substitution sites in the Li-ion conductors. The number of initial candidate compounds substituted with different elements across the periodic table in A site (blue) or M site (red) of (b) NASICON and (c) garnet.

sites. M and M' represent a pair of transition metal cations, selected based on commonly observed oxidation states. We systematically enumerate substitutional compositions by varying the Li content x between 1.0 to 3.0 with increments of 0.5 and by considering all possible $M_yM'_{1-y}$ cation pairs within the transition metal species set. The average valence state of $M_yM'_{1-y}$ is constrained between 2+ and 6+, incremented by 0.25. Overall charge neutrality is achieved by combining different mixtures of polyanion groups with diverse formal charges, including $(PO_4)^{3-}$, $(SO_4)^{2-}$, $(SiO_4)^4$, $(VO_4)^{3-}$, and $(MoO_4)^{2-/3-}$. To include both SSEs and MIECs, we sample a vast range of substitutions of the M site, including both redox-inactive single-valent and multi-valent cations that can undergo redox, resulting in 313,217 compositions in total. The substituted elements and their allowed valence states for NASICON are presented in the periodic table in Figure 2(b). The color intensity indicates the number of compounds in our set that contain this element either on the M site (blue) or on the A site (red).

For garnet compounds, we adopt the crystal structures with $Ia\bar{3}d$ symmetry with the chemical formula $Li_xLa_3(M_yM'_{1-y})_2O_{12}$, where x ranges from 3.0 to 7.0 in increments of 0.5. Similar to NASICON, M and M' denote transition metal cations in different oxidation states, with the average oxidation state of $M_yM'_{1-y}$ constrained between 2+ and 6+ in steps of 0.25. We only substitute the octahedral M site while fixing La^{3+} in the dodecahedral site. A total of 6,823 La-based garnet candidates are generated, with their elemental distribution shown in Figure 2(c). Although the initial number of garnet candidates is considerably smaller than that of NASICONs, we show below that the pass rate of garnet compounds while screening is substantially higher, yielding a comparable number of final candidates: 121 SSEs and 7 MIECs for garnet, versus 74 SSEs and 7 MIECs for NASICON. This high pass rate for the garnet compounds suggests a generally greater alkaline stability of garnets

relative to NASICONs, as discussed in later sections.

B. Stability metrics

In this section, we explain how we quantify the potential synthesizability of the candidate materials, as well as their stability against the harsh environments in humid Li-air systems. To exclude highly unstable compounds that are unlikely to be synthesized, we calculate the energy above the convex hull (E_{hull}) for each candidate. Although reasonably low E_{hull} is not a sufficient condition for the successful synthesis of a hypothetical material, it serves as an efficient and widely used metric for ruling out highly unstable materials and serves as a rough proxy of the synthesizability of a material [37–39].

In addition to E_{hull} , we assess the driving force for three distinct parasitic reactions that can degrade the material as illustrated in Figures 3(a-d). We evaluate the electrochemical stability against the applied voltages, using the previously developed approach [10, 40, 41], and calculate the electrochemical stability window for each candidate. The upper and the lower limits correspond to the oxidation (V_{ox}) and the reduction (V_{red}) limits, respectively (Figure 3 (a)). We apply two modifications to the general approach [10, 41] for the estimation of the electrochemical window. (1) In theory a metastable material $(E_{hull} > 0 \text{ meV/atom})$ has no electrochemically stable window as thermodynamics would predict its decomposition to its competing phases even without voltage applied. However, metastable materials often exhibit certain stability against oxidation and reduction, which can be due to various reasons, including slow kinetics of decomposition at room temperature, thermal stabilization, and formation of passivating decomposition products on the surface, etc. To obtain an optimistic estimation of the electrochemical stability window of a metastable compound, we vertically shift the energy of the metastable target compound, breaking the

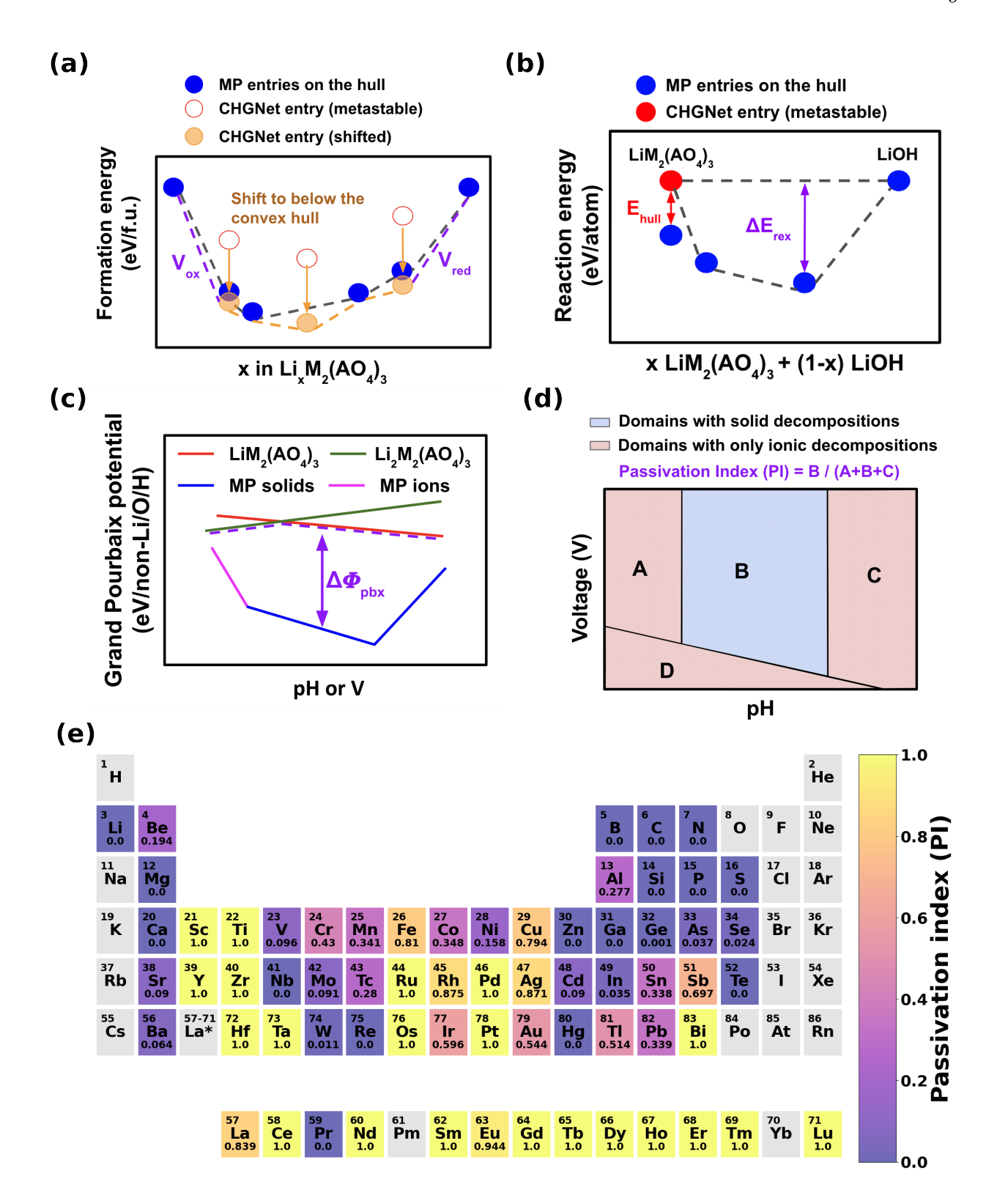


FIG. 3. Schematic plot of stability metrics (a) V_{ox} and V_{red} for electrochemical stability. (b) E_{rex} for chemical stability. (c) $\Delta\phi_{pbx}$ and (d) passivation index (PI) for alkaline stability. (e) Elemental PI across the periodic table. In Figures (a-c), NASICON compounds $\text{Li}_x\text{M}_2(\text{AO}_4)_3$ are assumed for demonstration purpose, but the stability metrics are similarly defined for garnet compounds $\text{Li}_x\text{La}_3\text{M}_2\text{O}_{12}$ as well.

convex hull at the corresponding composition (either at the stable decomposition on the hull or on the tie line between the nearest neighbor stable compositions) by a small amount (10 meV/atom for CHGNet pre-screening step, and 1 meV/atom for DFT-screening step). The resulting electrochemical window represents the upper (lower) limits of the true thermodynamic oxidation (reduction) limits. (2) Redox-active compounds can undergo topotactic lithium insertion and extraction reactions instead of decomposition reactions [42]. As the topotactic reaction maintains the host crystal framework, we do not consider this a "breakdown" of a material. Thus, we assume that the topotactic Li insertion and extraction is kinetically accessible for topotactically related compositions. Therefore, the oxidation (or reduction) limit of a redox-active compound is defined as the maximum (or minimum) of all oxidation (or reduction) limits among all topotactically related compositions with different Li contents.

During the battery operation, the surfaces of SSE and MIEC cathode are exposed to H_2O and LiOH. H_2O is naturally present due to the exposure of the cathode to humid air, while LiOH is a discharge product on the surfaces of SSE or MIEC cathode. We compute the driving force for the chemical reaction between our candidate compounds and H_2O or LiOH. As shown in Figure 4(c), the reaction product and the corresponding reaction energy depend on the ratio between the two reactants. Similar to concepts used in solid-state reaction theory [43], we use the most negative reaction energy per reactant atom as an indicator of the driving force for our candidate materials to chemically react with H_2O or LiOH, referring to it as ΔE_{rex} . Since ΔE_{rex} is referenced to the reactants, a spontaneous reaction will have a negative value of ΔE_{rex} .

The formation of LiOH as the discharge product in the humid environment inevitably creates a high pH environment due to the hydrophilic nature of LiOH. Therefore, the Li-

the dissolution of many species. In our screening, the alkaline stability is evaluated by constructing Pourbaix diagrams for each candidate compound [44]. A Pourbaix diagram shows whether the target compound is stable, or if not, which set of thermodynamically most stable decomposition products (either solid, ions in solution, or the combination of both) form at a given pH and voltage. In the Pourbaix diagram, the stability of the target compound at a given pH and voltage is quantified by the so-called Pourbaix potential (ψ_{pbx}) [45, 46]. The difference in the Pourbaix potential between the target compound and the most stable decomposition phases (either solid phases or ionic solution species) is called the Pourbaix decomposition energy, which measures the thermodynamic driving force to decompose in a given pH and voltage condition [47]. Different to ΔE_{rex} vs. LiOH, where only solid phases are taken into consideration, the Pourbaix decomposition energy is evaluated including both solid phases and ionic solution species within a given chemical space, and thus, it better describes the stability of materials in a solution environment.

Conventionally, the Pourbaix diagram assumes that the system is open to oxygen, protons, and electrons, as these species can be delivered or absorbed by the oxidation/reduction reactions in water. As a result, the Pourbaix potential has a unit of energy per non-O/H atoms (eV/non-O/H). Here, in order to simulate the alkaline stability of both SSE and MIEC compounds during the battery operation with varying lithium chemical potential, we further assume that the system is also open to Li⁺ exchange, in which case the Pourbaix potential has a unit of energy per non-Li/O/H atoms (eV/non-Li/O/H). To differentiate it from the conventionally calculated Pourbaix potential, we refer to the new potential as the grand Pourbaix potential (ϕ_{pbx}). This newly-defined grand Pourbaix potential is particularly useful for estimating the alkaline stability of compounds where Li⁺ can be topotactically in-

serted or extracted from the host structure as the voltage varies during charge and discharge. As demonstrated in Figure 4(d), the grand Pourbaix potential of these topotactically related compositions can be evaluated simultaneously in the same Pourbaix diagram. At each pH and voltage condition, the Li content of a given non-Li composition is determined as the one with the lowest ϕ_{pbx} . Following the convention in Ref [47], the value of $\Delta \phi_{pbx}$ is referenced to the most stable phases, and therefore, any metastable compound will have positive values of $\Delta \phi_{pbx}$. We use the maximum of the grand Pourbaix decomposition energy (max $\Delta \phi_{pbx}$) within the battery operating window (pH = 12 - 15 and voltage = 2.0 - 4.2 V vs. Li/Li⁺) as an indicator for alkaline stability. The candidate material with lower max $\Delta \phi_{pbx}$ is considered to be more resistant to the corrosive alkaline environment.

That being said, a material with a high max $\Delta\phi_{pbx}$ value does not necessarily imply the material always severely degrades. It was previously demonstrated that the degradation of a material can be potentially mitigated if the decomposition products can act as an effective corrosion-resistive solid passivation layer [47]. Passivation is controlled by a series of chemical and mechanical effects on the surface and cannot be exactly predicted with any models [48–51]. In this work, we therefore estimate the passivation capability of candidate compounds by a passivation index (PI). PI is defined as the fractional area of the domains in the Pourbaix diagram where at least one solid decomposition product forms within the battery operation window (pH = 12 - 15 and voltage = 2.0 - 4.2 V vs. Li/Li⁺). A higher PI value indicates a higher chance that the surface can be covered by a solid passivation layer and be protected from further dissolution. In practice, a solid product may not always function as a stable passivation layer [52, 53]. Therefore, PI can be seen as the best-case estimation of the passivation capability of a given composition.

The PI of each element's individual Pourbaix diagram is shown in Figure 3 (e) and

provides useful information about the passivation capability of each element. As can be seen, there is a large variation in the elemental PI across the periodic table. Some elements, such as early transition metals (TMs) and the lanthanide series, have very high PI close to 1.0, whereas others, including alkaline earth metals and first-row 3d TMs, exhibit negligible passivation capability with PI values approaching 0.0. According to our definition, the PI for a compound will always be equal or greater than that of the consisting element in the compound with the highest PI. This is because different elements in a compound can form different solid decomposition products at different pH and voltage conditions. It is also possible that multiple elements form a compound-type decomposition product. Therefore, elements with low elemental PI can be co-substituted with those having high elemental PI to increase the overall PI of the compound. Our model implicitly assumes that, in the worst-case scenario, surface atoms with low elemental PI dissolve into the solution, whereas the remaining atoms with high elemental PI will accumulate and form a passivation layer on the surface. Elemental La exhibits a high PI value of 0.84, and other elements in the lanthanide series show even higher values. This suggests that lanthanides generally offer strong passivation capabilities and are unlikely to be the limiting factor for passivation in garnet materials.

C. Hierarchical high-throughput screening scheme

Figure 4 illustrates the hierarchical screening scheme that combines the use of the CHGNet model [36] and DFT. CHGNet is a universal machine-learning interatomic potential (uMLIP) model pretrained on the MPtrj dataset, which consists of over 1.5 million inorganic materials calculated by the Materials Project (MP) team with DFT [54, 55]. The CHGNet model has previously been shown to have reasonable accuracy in studying Li-ion

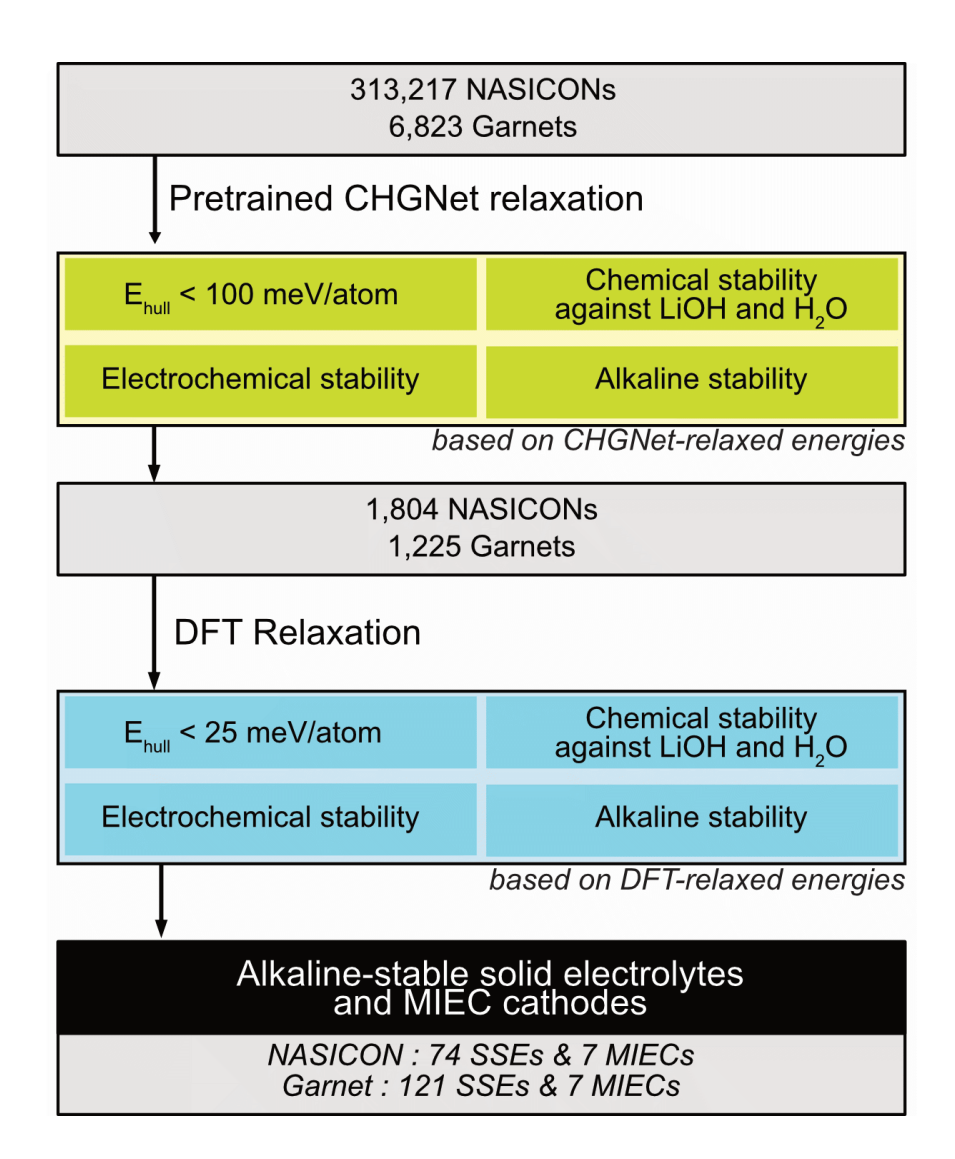


FIG. 4. 2-step hierarchical screening scheme combining MLIP and DFT calculations We use pretrained CHGNet to relax all initial candidate compounds in the pre-screening step. DFT relaxations are performed on the subset of candidates that pass the pre-screening step.

conductors [56, 57]. We apply the CHGNet model for a fast pre-screening, followed by higher fidelity DFT calculations on a selected subset of compounds. Starting with 313,217 and 6,823 candidates with NASICON and garnet structures, we perform structure relaxation using the pretrained CHGNet. In the pre-screening step, energy above hull is computed by comparing the CHGNet-relaxed energy with the convex hull constructed from all competing phases available in the MP. Compounds with $E_{hull} < 100 \text{ meV/atom}$ are selected for further evaluation of their chemical, electrochemical, and alkaline stabilities (see Methods

for detailed screening criteria). This pre-screening step yields 1,804 NASICON and 1,225 garnet candidate compounds. In the subsequent DFT-screening step, we re-relax the pre-screened candidates with DFT calculations. The energy above hull is reevaluated using the DFT-relaxed energy, and the candidates are further downselected with a tighter criterion $E_{hull} < 25 \text{ meV/atom}$. For the compounds that meet this criterion, we recalculate chemical, electrochemical, and alkaline stabilities using the DFT-relaxed energies. The screening criteria of chemical, electrochemical, and alkaline stabilities for NASICON and garnet compounds differ slightly between the CHGNet pre-screening and DFT downselection steps. The specific criteria, along with the rationale behind them are detailed in Tables IV and III in the Methods section. Our hierarchical screening ultimately identifies 81 NASICON (74 SSEs and 7 MIECs) and 128 garnet (121 SSEs and 7 MIECs) compounds.

III. RESULTS

A. Distributions of stability metrics among all initial candidate compounds

The distributions of the stability metrics based on CHGNet-relaxed energies for both NASICON and garnet compounds are presented in Figure 5. In Figures 5 (a) and (b), the distribution of E_{hull} values are shown as a function of Li content per formula unit (x) for NASICON and garnet, respectively. Our screening results show that the distributions of E_{hull} for garnets has overall lower values than those of NASICONs. Such trend persists even when only phosphate-based NASICON compounds are considered (see Supplemental Information Figure S1). These results imply that La-based garnets may intrinsically be easier to substitute than NASICON compounds. We also observe that the trend that E_{hull} increases with lithium content x for both crystal frameworks, indicating a decrease of stability as more

Li is stuffed into the host structure. Typically, increasing Li content beyond the baseline content (x = 1 for phosphate-based NASICON and x = 3 for garnet) enhances Li-ion conductivity by creating activated local environments that diffuse with low barrier without getting trapped or dissipated[58]. For phosphate-based NASICON, the optimal conductivity was found to be in the range of 1.0 < x < 2.0 [2], while the range 6.0 < x < 7.0 is optimized for garnet [1]. Given that the E_{hull} range for experimentally synthesized oxide compounds can often reach up to ~ 60 meV/atom [59], our screening results reveal that there are potentially many undiscovered Li-stuffed NASICON and garnet compounds that are synthesizable and promising as new Li-ion conductors.

For all compounds with CHGNet-calculated $E_{hull} < 100 \text{ meV/atom}$, we show the distribution of electrochemical stability, characterized by V_{ox} and V_{red} in Figure 5 (c) and (f) for NASICONs and garnets, respectively. Our analysis shows that NASICONs have higher values for both V_{ox} and V_{red} than garnets, suggesting that NASICONs are more stable against oxidation, whereas garnets are superior in terms of the stability against reduction, consistent with previous theoretical and experimental studies [10, 60]. The trend in V_{red} can be understood by the inductive effect of the polyanion groups in NASICONs [61]. The strong covalent bonds within the polyanion unit lowers the covalency of the bonds between the octahedral-site cation and the surrounding oxygen anions, leading to an increase in the potential of the redox couple vs. Li/Li⁺. Similarly, the oxidation of the oxygen anion, which usually is the breakdown mechanisms for oxide SSE at high voltages is moved to higher voltage by its covalent bonding in the polyanion groups [61]. As our target voltage range is 2.0 - 4.2 V vs. Li/Li⁺, the compositional optimization should aim to lower the reduction limit for NASICON and raise the oxidation limit for garnet.

The chemical stability against side reactions is quantified by the reaction energy (ΔE_{rex})

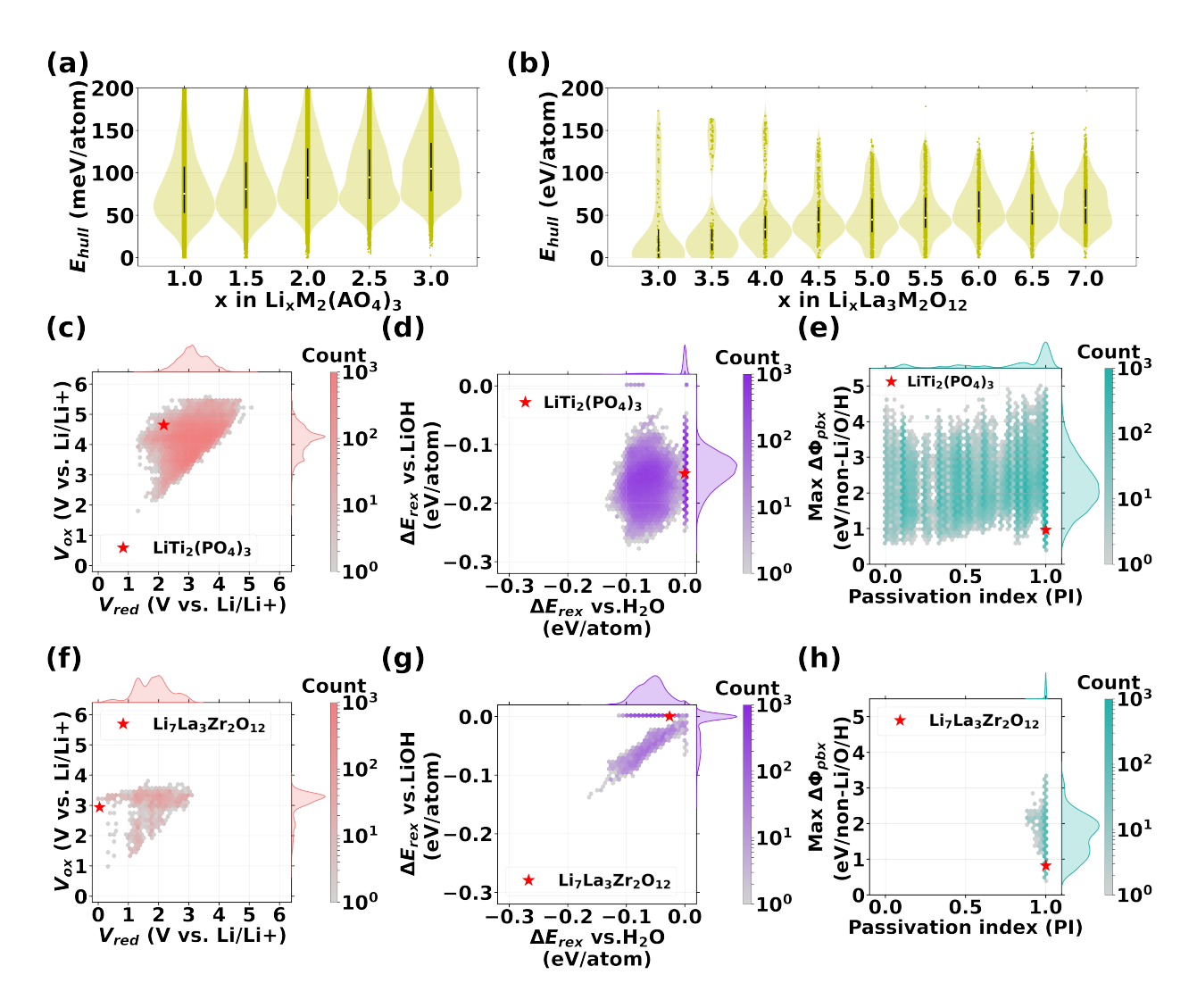


FIG. 5. Distributions of stability metrics based on CHGNet-relaxed energies Synthesizability (E_{hull}) for (a) NASICON and (b) garnet. (c) electrochemical stability (V_{ox} and V_{red}), (d) chemical stability (ΔE_{rex} vs. H₂O or LiOH), and (e) alkaline stability ($\max \Delta \phi_{pbx}$ and PI) of NASICONs. The corresponding distributions for garnets are shown in (f-h). In (c-h), only the compounds with $E_{hull} < 100$ meV/atom are included. The data points for LiTi₂(PO₄)₃ and Li₇La₃Zr₂O₁₂ shown in (c-h) are obtained by using their DFT-relaxed energies for higher accuracy.

between the given Li-ion conductors and chemical species prevalent in the environment, namely H_2O and LiOH. As can be seen in Figure 5 (d) and (g), garnet compounds tend to be more reactive against H_2O with a ΔE_{rex} magnitude peaking at \sim -0.05 eV/atom, while NASICON compounds show near zero reactivity against H_2O . In contrast, the majority of NASICON compounds easily react with the discharge product LiOH with ΔE_{rex} peaking at \sim -0.14 eV/atom, whereas garnets are much more stable against LiOH. The high reactivity

between NASICON and LiOH poses concerns for using NASICON-type compounds in a high pH environment. Indeed, experimental observation of the degradation of NASICON-type conductors in alkaline solutions has been previously reported [62–64].

The distribution of $\Delta\phi_{pbx}$ and PI values are plotted in Figures 5 (e) and (h). The results shown in Figure 5 indicate that most of the NASICON and garnet compounds have good passivation capabilities with the peak of the PI distribution near 1.0. We also find that the distribution of PI is much broader for NASICONs compared to garnets, indicating that the high passivation capability is more consistent among different garnet compounds, whereas it is more chemistry-dependent for NASICON. The driving force for decomposition in an alkaline medium peaks near max $\Delta\phi_{pbx} = \sim 2.0 \, \text{eV/non-Li/O/H}$ for both crystal frameworks. However, the distribution for garnet is slightly narrower and skews more towards lower max $\Delta\phi_{pbx}$ values compared to that of NASICON. Both the narrower PI distribution and the lower max $\Delta\phi_{pbx}$ values indicate that garnet compounds would generally be less prone to degradation in an alkaline environment compared to NASICON.

For comparison, the stability metrics for the prototype compounds of NASICON (LiTi₂(PO₄)₃, LTPO) and garnet (Li₇La₃Zr₂O₁₂, LLZO) are also calculated using DFT, which are labeled as red stars in the Figures 5 (c-h). These prototype compounds show contrasting behavior in terms of electrochemical and chemical stabilities: while LTPO is more stable against oxidation with higher V_{ox} of 4.6 V, LLZO has V_{red} close to zero, indicating the significant stability of LLZO against Li metal [10]; LTPO is more reactive with LiOH with Δ E_{rex} = -0.15 eV/atom, while it remains stable against H₂O with zero reaction energy. Conversely, LLZO spontaneously reacts with H₂O with Δ E_{rex} = -0.03 eV/atom, but it is stable against LiOH with zero reaction energy. These results on electrochemical and chemical stabilities align with the trend observed across all NASICON and garnet compounds. As for alka-

line stability, both LTPO and LLZO show similar passivation behavior with PI = 1.0 for both compounds. Also, both LTPO and LLZO have low max $\Delta\phi_{pbx}$ values of 1.0 and 0.8 eV/non-Li/O/H, respectively. The distributions shown in Figure 5 indicate the presence of numerous compounds that may potentially have superior stability compared to LTPO and LLZO, characterized by less negative Δ E_{rex} values, higher oxidation and lower reduction limits, and less positive max $\Delta\phi_{pbx}$ values. These NASICON and garnet compounds are first filtered based on the screening criteria for CHGNet pre-screening step, and further downselected using DFT-relaxed energies (see Tables IV and III in the Methods section), yielding 81 NASICON and 128 garnet compounds as the final candidates.

B. Final list of compounds as candidate SSE and MIEC materials

The final NASICON and garnet compounds that pass all the screening filters in Figure 4 are further categorized into possible SSE or MIEC cathodes based on their Li-insertion redox potential. More specifically, we assume that a compound that is redox-active within the battery operation voltage window $(2.0 - 4.2 \text{ V vs. Li/Li}^+)$ can potentially exhibit a reasonable electronic conductivity via a polaron hopping mechanism [69, 70] between the mixed valence states present. The effectiveness of substituting redox-active TMs to enhance electronic conductivity of an originally redox-inactive SSE has been previously experimentally validated. For instance, increases in electronic conductivity by 4 and 3 orders of magnitude were achieved for garnet-type [71] and NASICON-type [72] Li-ion conductors, respectively. We estimate the redox activity by calculating the average Li intercalation voltages between the topotactically related compositions. Specifically, if there are any Li intercalation voltages that fall within the voltage range of $2.0 - 4.2 \text{ V vs. Li/Li}^+$, the topotactically related compositions are grouped and categorized as a MIEC. Otherwise, the

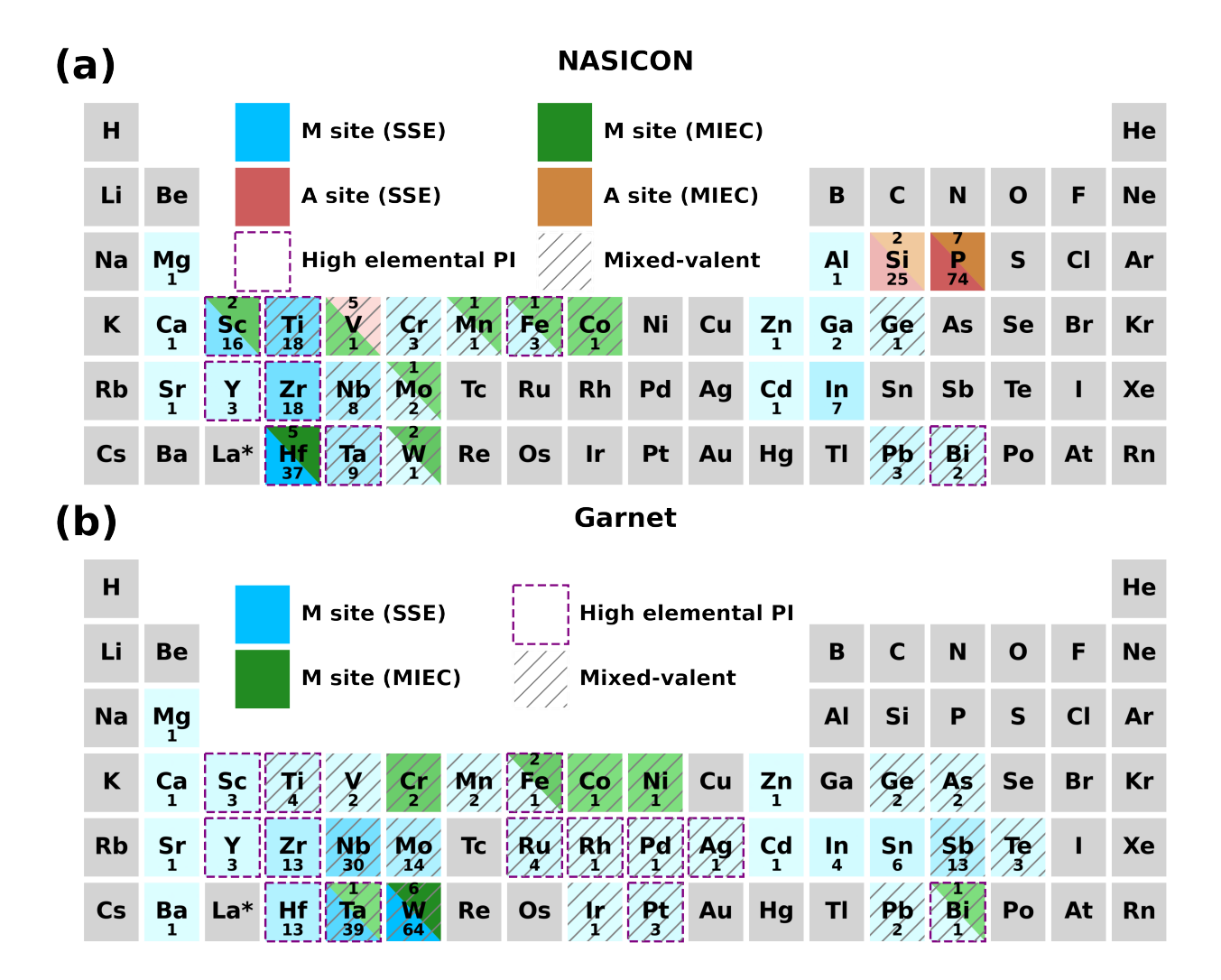


FIG. 6. Elements selected in the final candidate compounds (a) Substituted elements in M and A sites among 74 SSE and 7 MIEC candidates with NASICON framework. (b) 121 SSE and 7 MIEC candidates with garnet framework. M-site substitutions are shown in blue and green for SSE and MIEC compounds, respectively. A-site substitutions are shown in red and brown for SSE and MIEC compounds, respectively. The elements with high elemental PI (PI > 0.8) are highlighted with dashed purple lines around the boxes. The mixed-valent elements are highlighted with green slashes inside the boxes. The number in each elemental box represents the number of final candidate compounds that contain the corresponding element. All topotactically related compositions that only differ by Li content are grouped and counted as one MIEC compound.

composition is considered to be redox-inactive and categorized as a SSE. In theory, the redox-active MIEC cathodes can provide extra Li storage capacity, though this is not our primary objective.

We obtain 74 SSE and 7 MIEC candidates for NASICON, and 121 SSE and 7 MIEC candidates for garnet. All elements selected in these final candidates are presented in pe-

TABLE I. A subset of the final screened NASICON candidates All identified NASICON MIECs and 10 out of the 74 final NASICON SSE candidates are tabulated here. Only the lowest E_{hull} value among different Li contents is listed for each MIEC compound with varying Li-content, where the corresponding Li content is indicated in the parenthesis. The parenthesis in the Li intercalation voltage indicates the range of lithium content at which its corresponding voltage lies outside the battery operating window $(2.0 - 4.2 \text{ V vs. Li/Li}^+)$. The Li-ion conductivity at 300 K is evaluated by performing molecular dynamics simulations using a fine-tuned CHGNet model. The numbers in brackets are the upper and lower limit estimation of the Li-ion conductivity, and the error for activation energy represents the standard deviation value [65]. For each MIEC compound, Li-ion conductivity is evaluated only at the composition specified in parenthesis. This composition meets all DFT-screening criteria and has a Li content x closest to 1.5, which has been experimentally shown to yield higher Li-ion conductivity [2].

Compound	E_{hull} (meV/atom)	$\begin{array}{c} {\rm Max} \ \Delta \phi_{pbx} \\ {\rm (eV/non\text{-}Li/O/H)} \end{array}$	Li intercalation voltage (V)	Li-ion conductivity at 300 K (mS/cm)	Activation energy (eV)	Category
${\rm LiTi_2(PO_4)_3}$	0	0.963	(Li ₁ -Li ₃ : 1.5)	$0.07 \; (Exp.)^{a}$	0.47 (Exp.) ^a	Baseline SSE
$\rm Li_3Sc_2(PO_4)_3$	14	0.497	None	2e-4, [6e-5, 8e-4]	0.560 ± 0.031	SSE
$\rm LiTa_2Si_2PO_{12}$	16	0.579	None	2e-4, [4e-5, 7e-4]	0.560 ± 0.034	SSE
$\rm Li_2Hf_{1.5}Sc_{0.5}Si_{0.5}P_{2.5}O_{12}$	17	0.580	None	1.4, [0.9, 2.2]	0.288 ± 0.010	SSE
$\rm Li_{1.5}Hf_2Si_{0.5}P_{2.5}O_{12}$	2	0.596	None	$3.2,[2.1,\ 4.9]$	0.243 ± 0.010	SSE
$\mathrm{LiTa_{5/3}Nb_{1/3}Si_2PO_{12}}$	19	0.602	None	4e-5,[9e-6, 2e-4]	0.605 ± 0.038	SSE
$\rm Li_{2.5}Hf_{0.5}Sc_{1.5}(PO_4)_3$	22	0.603	None	3.2, [2.2, 4.8]	0.260 ± 0.009	SSE
$\rm Li_{1.5}Y_{0.5}Hf_{1.5}(PO_4)_3$	1	0.608	None	0.2, [0.1, 0.4]	0.338 ± 0.013	SSE
$\mathrm{LiTa}_{1.5}\mathrm{Nb}_{0.5}\mathrm{Si}_{2}\mathrm{PO}_{12}$	20	0.613	$(\text{Li}_1\text{-Li}_{1.5}: 1.1)$ $(\text{Li}_{1.5}\text{-Li}_2: 0.6)$	7e-5, [2e-5,3e-4]	0.595 ± 0.035	SSE
$\rm Li_3ScIn(PO_4)_3$	14	0.613	None	6e-5, [1e-5, 4e-4]	0.601 ± 0.042	SSE
$\mathrm{Li_{1.5}HfZrSi_{0.5}P_{2.5}O_{12}}$	13	0.620	None	1.2, [0.7, 1.8]	0.282 ± 0.011	SSE
$\rm Li_xHf_{1.5}W_{0.5}SiP_2O_{12}$	16 (Li _{1.5})	0.775	Li ₁ -Li _{1.5} : 3.1 (Li _{1.5} -Li ₂ : 1.9)	0.7, [0.4, 1.1] (Li _{1.5})	0.301 ± 0.011 (Li _{1.5})	MIEC
$\rm Li_x Hf_{1.5} Fe_{0.5} (PO_4)_3$	$0 (Li_{1.5})$	0.846	$(\text{Li}_1\text{-Li}_{1.5}: 4.8)$ $\text{Li}_{1.5}\text{-Li}_2: 2.5$	7.2, $[4.8, 10.8]$ (Li _{1.5})	0.217 ± 0.010 (Li _{1.5})	MIEC
$\rm Li_xHf_{1.5}Co_{0.5}(PO_4)_3$	9 (Li _{1.5})	0.865	$(\text{Li}_1\text{-Li}_{1.5}: 4.7)$ $\text{Li}_{1.5}\text{-Li}_2: 3.8$	7.3, $[4.9, 11.0]$ (Li _{1.5})	0.216 ± 0.010 (Li _{1.5})	MIEC
$\rm Li_xSc_{1.5}W_{0.5}(PO_4)_3$	$23 (Li_2)$	0.907	Li _{1.5} -Li ₂ : 3.1 Li ₂ -Li _{2.5} : 2.7	6.0, [3.9, 9.2] (Li _{1.5})	0.209 ± 0.010 (Li _{1.5})	MIEC
$\rm Li_xSc_{1.5}Mo_{0.5}(PO_4)_3$	13 (Li ₃)	0.934	Li _{1.5} -Li ₂ : 3.5 Li ₂ -Li _{2.5} : 3.4	1.0, [0.6, 1.6] (Li ₂ ^b)	0.302 ± 0.011 (Li ₂ ^b)	MIEC
$\rm Li_xHf_{1.5}Mn_{0.5}(PO_4)_3$	$0 \; (\mathrm{Li}_{1.5})$	1.041	(Li ₁ -Li _{1.5} : 4.3) Li _{1.5} -Li ₂ : 3.1	1.7, [1.1, 2.7] ($\text{Li}_{1.5}$)	0.274 ± 0.011 (Li _{1.5})	MIEC
$\rm Li_x Hf_{1.5} V_{0.5} Si_{0.5} P_{2.5} O_{12}$	16 (Li ₂)	1.063	$\text{Li}_{1}\text{-Li}_{1.5}$: 3.7 $\text{Li}_{1.5}\text{-Li}_{2}$: 3.1 ($\text{Li}_{2}\text{-Li}_{2.5}$: 1.3)	5.3, [3.6, 7.9] (Li _{1.5})	0.231 ± 0.010 (Li _{1.5})	MIEC

^a The experimental conductivity data is obtained from [66, 67]

^b The composition with x = 1.5 (Li_{1.5}Sc_{1.5}Mo_{0.5}(PO₄)₃) has $E_{hull} = 28$ meV/atom, which exceeds the DFT-screening cutoff value (25 meV/atom), and thus is not selected for the MD simulations

TABLE II. A subset of the final screened garnet candidates All identified garnet MIECs and 11 out of the 121 final garnet SSE candidates are tabulated here. For each MIEC compound, Li-ion conductivity is evaluated only at the composition specified in parenthesis. This composition satisfies all DFT-screening criteria and has a Li content x closest to 7.0, which has been experimentally shown to yield higher Li-ion conductivity [1] in garnet. For additional details, refer to Table I.

	E_{hull}	$\operatorname{Max} \Delta \phi_{pbx}$	Li intercalation	Li-ion conductivity	Activation	
Compound		$\frac{\Delta \phi_{pbx}}{\text{(eV/non-Li/O/H)}}$	voltage (V)	at 300 K (mS/cm)	energy (eV)	Category
$\rm Li_7La_3Zr_2O_{12}$	7	0.822	None	0.31 (Exp.) ^a	0.34 (Exp.) ^a	Baseline SSE
$\rm Li_3La_3W_2O_{12}$	0	0.282	$(\text{Li}_3\text{-Li}_5: 1.1)$ $(\text{Li}_5\text{-Li}_7: 0.9)$	None	None	SSE
$\rm Li_{3.5}La_{3}Ta_{0.5}W_{1.5}O_{12}$	0	0.330	(Li _{3.5} -Li _{4.5} : 1.2) (Li _{4.5} -Li ₅ : 1.1) (Li ₅ -Li _{6.5} : 0.9) (Li _{6.5} -Li ₇ : 0.8)	1.3, [0.7, 2.4]	0.233 ± 0.015	SSE
$\rm Li_{3.5}La_{3}Nb_{0.5}W_{1.5}O_{12}$	0	0.340	(Li _{3.5} -Li _{4.5} : 1.2) (Li _{4.5} -Li ₅ : 1.1) (Li ₅ -Li _{6.5} : 0.9) (Li _{6.5} -Li ₇ : 0.6)	1.7, [0.9, 3.3]	0.222 ± 0.016	SSE
$\rm Li_4La_3TaWO_{12}$	0	0.363	$(\text{Li}_4\text{-Li}_5: 1.1)$ $(\text{Li}_5\text{-Li}_6: 0.8)$	0.2, [0.1, 0.4]	0.323 ± 0.016	SSE
$\rm Li_4La_3NbWO_{12}$	0	0.382	(Li ₄ -Li ₅ : 1.1) (Li ₅ -Li ₆ : 0.72) (Li ₆ -Li ₇ : 0.70)	0.3, [0.1, 0.5]	0.319 ± 0.014	SSE
$\rm Li_5La_3Ta_2O_{12}$	8	0.397	None	3.9, [2.5, 6.3]	0.228 ± 0.011	SSE
${\rm Li}_5{\rm La}_3{\rm Ta}_{1.75}{\rm Nb}_{0.25}{\rm O}_{12}$	9	0.408	None	1.9, [1.2, 3.2]	0.260 ± 0.012	SSE
$\mathrm{Li_6La_3Sc_{0.5}Ta_{1.5}O_{12}}$	23	0.624	None	2.5, [1.6, 4.1]	0.246 ± 0.012	SSE
$\rm Li_6La_3ZrTaO_{12}$	17	0.644	None	5.6, [3.5, 8.8]	0.210 ± 0.010	SSE
$\rm Li_{6.5}La_{3}Zr_{1.5}Ta_{0.5}O_{12}$	12	0.728	None	10.7, [7.1, 16.4]	0.188 ± 0.010	SSE
$\rm Li_{6.5}La_{3}Hf_{1.5}Ta_{0.5}O_{12}$	15	0.732	None	13.1, [8.5, 20.2]	0.178 ± 0.010	SSE
$\rm Li_{x}La_{3}Cr_{0.25}W_{1.75}O_{12}$	0 (Li _{3.5})	0.464	Li ₃ -Li _{3.5} : 2.8 (Li _{3.5} -Li _{4.5} : 1.8) (Li _{4.5} -Li ₅ : 1.2) (Li ₅ -Li _{5.5} : 1.11) (Li _{5.5} -Li _{6.5} : 1.09) (Li _{6.5} -Li ₇ : 1.0)	1.6, [0.9, 2.9] (Li _{3.5})	0.230 ± 0.014 (Li _{3.5})	MIEC
$\mathrm{Li_{x}La_{3}Fe_{0.25}W_{1.75}O_{12}}$	0 (Li ₄)	0.530	Li _{3.5} -Li _{4.0} : 2.0 (Li ₄ -Li _{4.5} : 1.2) (Li _{5.5} -Li ₇ : 1.1)	0.3, [0.2, 0.7] (Li _{4.0})	0.284 ± 0.017 (Li ₄)	MIEC
$\mathrm{Li_{x}La_{3}Ni_{0.25}W_{1.75}O_{12}}$	1 (Li ₄)	0.572	Li _{3.5} -Li ₄ : 3.1 (Li ₄ -Li _{5.5} : 1.2) (Li _{5.5} -Li ₇ : 1.1)	9e-3, [2e-3, 5e-2] (Li ₄)	0.402 ± 0.040 (Li ₄)	MIEC
$\mathrm{Li_{x}La_{3}Ta_{1.75}Bi_{0.25}O_{12}}$	7 (Li ₅)	0.582	Li ₅ -Li _{5.5} : 2.1	0.5, [0.3, 0.8] (Li _{5.5})	0.308 ± 0.013 (Li _{5.5})	MIEC
${\rm Li_x La_3 Co_{0.25} W_{1.75} O_{12}}$	0 (Li _{3.5})	0.583	Li _{3.5} -Li ₄ : 2.2 (Li ₄ -Li _{5.5} : 1.2) (Li _{5.5} -Li ₇ : 1.1)	4e-2, [2e-2, 0.1] (Li ₄)	0.351 ± 0.022 (Li ₄)	MIEC
$\rm Li_x La_3 Cr_{0.5} W_{1.5} O_{12}$	11 (Li ₄)	0.591	Li ₃ -Li _{3.5} : 3.0 Li _{3.5} -Li ₄ : 2.7 Li ₄ -Li _{4.5} : 2.4 (Li _{4.5} -Li ₆ : 1.2) (Li ₆ -Li _{6.5} : 1.12) Li _{6.5} -Li ₇ : 1.10	7e-2, [3e-2, 0.2] (Li _{4.5})	0.359 ± 0.022 (Li _{4.5})	MIEC
$\rm Li_xLa_3Fe_{0.5}W_{1.5}O_{12}$	8 (Li ₅)	0.676	Li ₄ -Li _{4.5} : 2.8 (Li _{4.5} -Li ₆ : 1.2) (Li ₆ -Li _{6.5} : 1.13) (Li _{6.5} -Li ₇ : 1.06)	0.3, $[0.1, 0.6]$ (Li _{4.5})	0.305 ± 0.016 (Li _{4.5})	MIEC

^a The experimental conductivity data is obtained from [68]

riodic tables in Figure 6. The number in each box indicates the number of final candidate compounds containing the corresponding element. The corresponding substitution site is labeled by colors, where the color is scaled according to the number in the box, with darker colors indicating a more frequent appearance of the particular element in the final candidates. As can be seen, the elements in the final candidates are not uniformly present across the periodic table. For NASICON, the early TMs, including Sc, Ti, Zr, and Hf, are selected more frequently as the cations to occupy the octahedral M site, while Nb, Ta, and W are favored for garnet. Also, all final NASICON candidates (74 SSEs and 7 MIECs) contain phosphate groups, with some of them substituted with silicate groups. The complete list of compositions and their predicted stabilities of all final SSE candidates are provided as Supplemental Information.

In Tables I and II, we list a subset of the final SSE candidates (10 NASICON SSEs and 11 garnet SSEs) and all MIEC candidates (7 NASICON MIECs and 7 garnet MIECs), along with their DFT-predicted properties. The baseline compounds LTPO and LLZO are also included in the table for comparison. The subset SSEs are selected as follows: For NASICON, the ten most alkaline-stable compounds with the lowest values of max $\Delta\phi_{pbx}$ are selected. For garnet, we selected 11 SSEs, which include the three most alkaline-stable garnets with the lowest max $\Delta\phi_{pbx}$ values among all SSEs, the two most alkaline-stable garnets with 4 Li per formula unit (Li4-garnet), the two most alkaline-stable garnets with 6 Li per formula unit (Li6-garnet), and the two most alkaline-stable garnets with 6.5 Li per formula unit (Li6-5-garnet). The high Li content garnet (Li content larger than 3.0) is intentionally included because the Li-stuffed garnets generally exhibit higher Li-ion conductivity [1, 58]. For this subset of final candidate compounds, we additionally calculated the room temperature Li-

ion conductivity with MD simulations using fine-tuned CHGNet models and the results are listed in the same Tables. The Li-ion conductivity result will be discussed more in detail in a later section.

The data in Table I shows that the maximum $\Delta\phi_{pbx}$ can be reduced up to 48% for a pure Sc-based NASICON compound Li₃Sc₂(PO₄)₃ compared to the baseline value of LTPO. An even more significant improvement is achieved for the garnet compounds (Table II), with the pure W-based garnet Li₃La₃W₂O₁₂ achieving the maximum decrease of 66% in max $\Delta\phi_{pbx}$ relative to the baseline value of LLZO. In the following discussion section, we provide more in-depth analyses of the screening results, rationalizing the origin of high alkaline stability of specific chemistries. Potential trade-offs between alkaline stability and other material properties will also be discussed, offering design principles for optimizing compositions to achieve multiple desirable material properties.

C. Effect of octahedral-site substitution on alkaline stability

Charge neutrality requires that not every cation can be substituted into each composition. For this reason, we plot in Figure 7 the average effect of the allowed cation pairs on the alkaline stability (max $\Delta \phi_{pbx}$) and synthesizability (E_{hull}). The cations are ordered along each axis based on the average values along each column or row. Therefore, in Figure 7 (a) and (c), the overall alkaline stability of the substituted compounds increases from the upper left corner to the lower right corner. Similarly, the E_{hull} increases, and thus the compound becomes less synthesizable from the upper left corner to the lower right corner in Figure 7 (b) and (d).

For NASICON, the results shown in Figure 7 (a) indicate that substituting early TMs, such as Y, Sc, Hg, Zr, and Ti, generally results in lower max $\Delta \phi_{pbx}$ values, and thus are

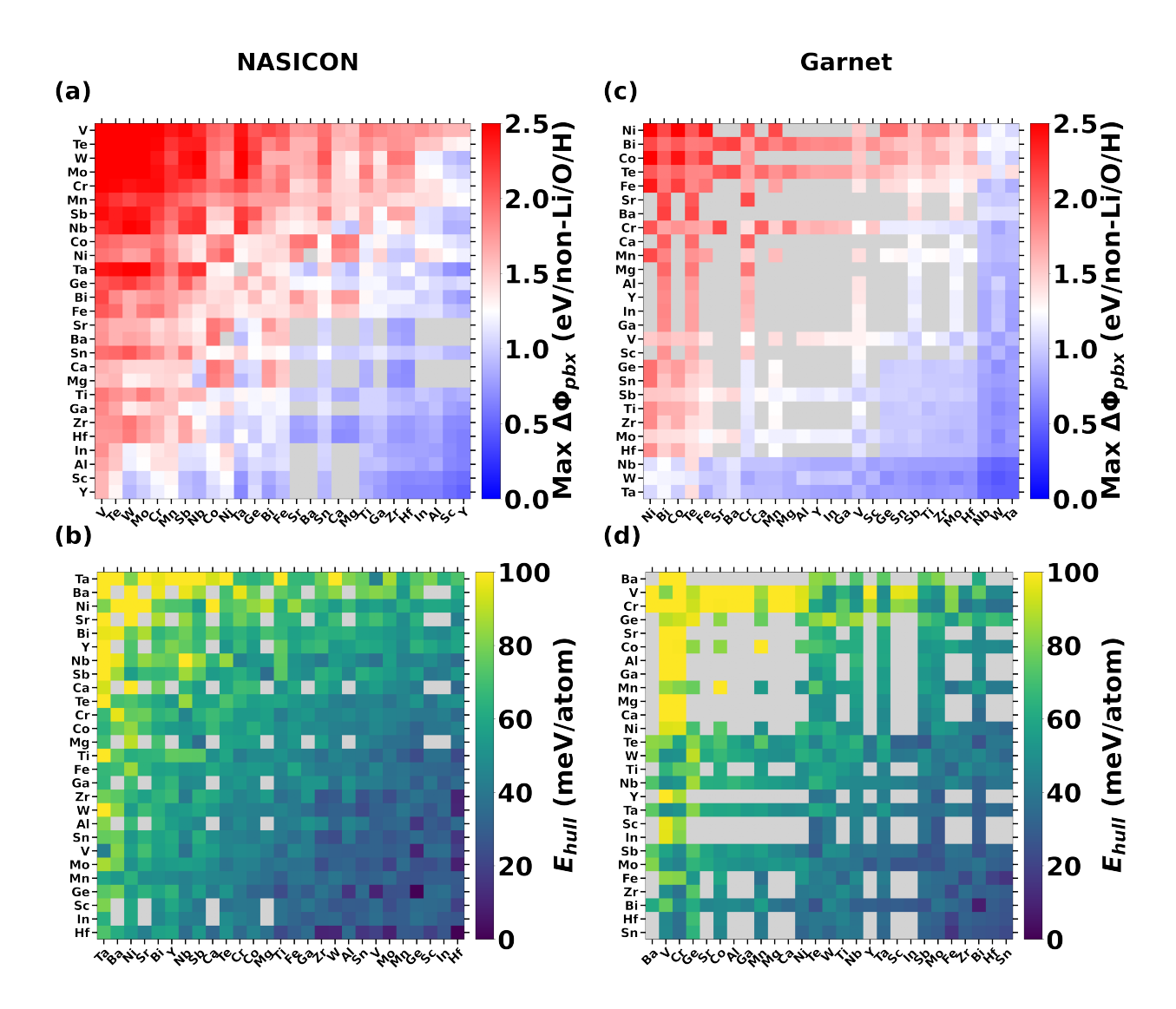


FIG. 7. Effect of the type of cation-pair in the octahedral site on stability The median values of max $\Delta\phi_{pbx}$ and E_{hull} for different cation pairs in the octahedral sites of NASICON are shown in (a) and (b), respectively. Similarly, the corresponding median values for garnet are shown in (c) and (d), respectively. Elements are ordered along the axes based on the average values along each column or row. Only phosphate-based NASICONs are considered in (a) and (b). For both NASICON and garnet, the median values of max $\Delta\phi_{pbx}$ in (a) and (c) are calculated by including only compounds with $E_{hull} < 100$ meV/atom to exclude intrinsically unstable compounds. If no compound with $E_{hull} < 100$ meV/atom exists for a given cation combination, the box is greyed out. Grey boxes in (b) and (d) indicate that the corresponding cation combinations are not considered in our screening due to violations of the compositional constraints on the range of Li content or charge neutrality. All values are based on CHGNet-relaxed energies.

beneficial for improving alkaline stability. In addition, all early TMs also have a high elemental PI of 1.0 (see Figure 3 (e)), indicating NASICON compounds substituted with early TMs can be potentially protected by the stable surface passivations in alkaline environment.

These early TMs are therefore also predominant in the final candidate list, as depicted in Figure 6 (a). The exception is for Y-based NASICONs: while we obtained more than 18 final candidates for Sc-, Hf-, Zr-, and Ti-based NASICONs, as shown in Figure 6 (a), only 3 Y-based NASICONs passed the final screening. The lower pass rate for Y-based NASICON originates from its relatively high E_{hull} value, which is evident from the lighter color shown in the column of Y in Figure 7 (b). Our DFT calculation indicates that $\text{Li}_3\text{Y}_2(\text{PO}_4)_3$ lies 66 meV/atom above the convex hull, being less stable than $\text{Li}_3\text{Sc}_2(\text{PO}_4)_3$, $\text{LiHf}_2(\text{PO}_4)_3$, $\text{LiZr}_2(\text{PO}_4)_3$, and $\text{LiTi}_2(\text{PO}_4)_3$ with E_{hull} value of 14, 0, 18, and 0 meV/atom respectively. To the best of our knowledge, the synthesis of $\text{Li}_3\text{Y}_2(\text{PO}_4)_3$ has not been experimentally reported so far.

Figure 7 (a) also shows that post-TM (Al, Ga, and In)-based NASICONs exhibit low max $\Delta\phi_{pbx}$, with Al- and In-based NASICONs ranking even higher than those based on Hf and Zr. However, these post-TMs are less common in final candidates compared to the compounds containing early TMs. This is due to the low elemental PI of these cations, as indicated by elemental PI values of 0.28, 0.0, and 0.04 for Al, Ga, and In, respectively in Figure 3 (e). Since phosphorus in the phosphate group does not provide any passivation capability with its elemental PI = 0.0, the NASICON compounds including post-TMs, such as Al, Ga, and In, must be paired with other cations with high elemental PI to have a stable surface passivation layer and to prevent continuous dissolution of the bulk material. Such chemistry-dependent passivation capability is the reason why we observe the broad distribution of PI for NASICON in Figure 5 (e).

Another interesting compositional category is the NASICONs based on alkaline earth metals (Mg, Ca, Sr, and Ba). Similar to the post-TMs, these alkaline earth metals also have low elemental PI values, with PI values of 0.0 for Mg, 0.0 for Ca, 0.09 for Sr, and

0.06 for Ba, as shown in Figure 3 (e). Therefore, alkaline earth metal are rare in the final NASICON candidate list, as shown in Figure 6 (a). However, as can be seen from Figure 7 (a), the NASICON compounds that are substituted with a combination of an alkaline earth metal and an early transition metal, such as Mg-Hf, Mg-Zr, and Mg-Ti cation pairs, have lower driving force for decomposition in an alkaline solution, with a value of max $\Delta \phi_{pbx}$ even lower than the pure Hf-, Zr-, and Ti-based NASICONs. According to our DFT calculations, the values of max $\Delta \phi_{pbx}$ are 0.595, 0.642, and 0.703 eV/non-Li/O/H for the compounds $Li_3MgHf(PO_4)_3$, $Li_3MgZr(PO_4)_3$, and $Li_3MgTi(PO_4)_3$, respectively. In comparison, the values of max $\Delta \phi_{pbx}$ for the pure early TM-based NASICONs are relatively higher, with values of 0.697, 0.753, and 0.963 eV/non-Li/O/H for $LiHf_2(PO_4)_3$, $LiZr_2(PO_4)_3$, and LiTi₂(PO₄)₃, respectively. On the other hand, the NASICON compounds based on these alkaline earth metals generally have high E_{hull} values, making these compounds likely more challenging to be synthesized. For instance, the DFT-estimated E_{hull} values are 26, 46, 32 for Li₃MgHf(PO₄)₃, Li₃MgZr(PO₄)₃, and Li₃MgTi(PO₄)₃, respectively, all of which exceed the 25 meV/atom cutoff in the DFT-screening step. Indeed, it was experimentally reported that solid-state synthesis of Li_{1+2x}Mg_xZr_{2-x}(PO₄)₃ series results in the formation of impurty phases for x > 0.2 [73]. This is another factor contributing to the scarcity of the alkaline earth metal-based NASICONs in the final candidate list. Nevertheless, the results presented above for both alkaline earth metal- and post-TM-based NASICONs indicate that while substituting low-PI elements might lead to a poorer passivation, it does not necessarily increase the driving force for decomposition in alkaline media (max $\Delta \phi_{pbx}$) and may even reduce it. The distributions of all types of stability metrics for each early TM, post-TM, and alkaline earth metal mentioned above are provided in Supplemental Information Figure S3.

Among the garnets, Figure 7 (c) shows that W-, Ta-, and Nb-based compounds have significantly lower values of max $\Delta\phi_{pbx}$ than compounds based on other cations. Similar to their beneficial effects on alkaline stability in NASICON, occupation of octahedral sites by the early TMs, such as Hf, Zr, and Ti, also tends to enhance the alkaline stability in garnet. Additionally, Mo- and Sb-based garnets also demonstrate alkaline stability comparable to the compounds with early TMs. These results are consistent with the final screening results shown in Figure 6(b), where W-, Ta-, and Nb-based garnets are the most common, followed by compounds containing early TMs (especially Hf, Zr, and Ti), as well as Mo and Sb. The distributions of all types of stability metrics for these elements that increases garnet's alkaline stability mentioned above are provided in Supplemental Information Figure S4.

In contrast to NASICON compounds, where conductors with low driving forces for decomposition in alkaline solution ($\Delta\phi_{pbx}$) typically contain early transition metals with high elemental PI values, many of the most common octahedral dopants in garnets exhibiting low $\Delta\phi_{pbx}$ have low elemental PI values. For instance, while Sb has a relatively high PI of 0.7, W, Nb, and Mo show much lower values of 0.01, 0.0, and 0.09, respectively (Figure 3e). All of these values are considerably lower than the early TMs (elemental PI = 1.0), and are also lower than the cutoff values (PI > 0.8) applied in both CHGNet pre-screening and DFT-screening steps. The high pass rate of these garnets substituted with elements having low elemental PI values can be attributed to the presence of La (elemental PI = 0.84) in the composition, which ensures that the compound PI remains high. This is evidenced by the narrow distributions of PI peaking near 1.0 across all La-based garnet compounds considered in our screening as shown in Figures 5 (h).

To better understand the underlying mechanisms for the low driving force for decomposition in alkaline solutions and the passivation mechanisms, we show in Figure 8 Pourbaix

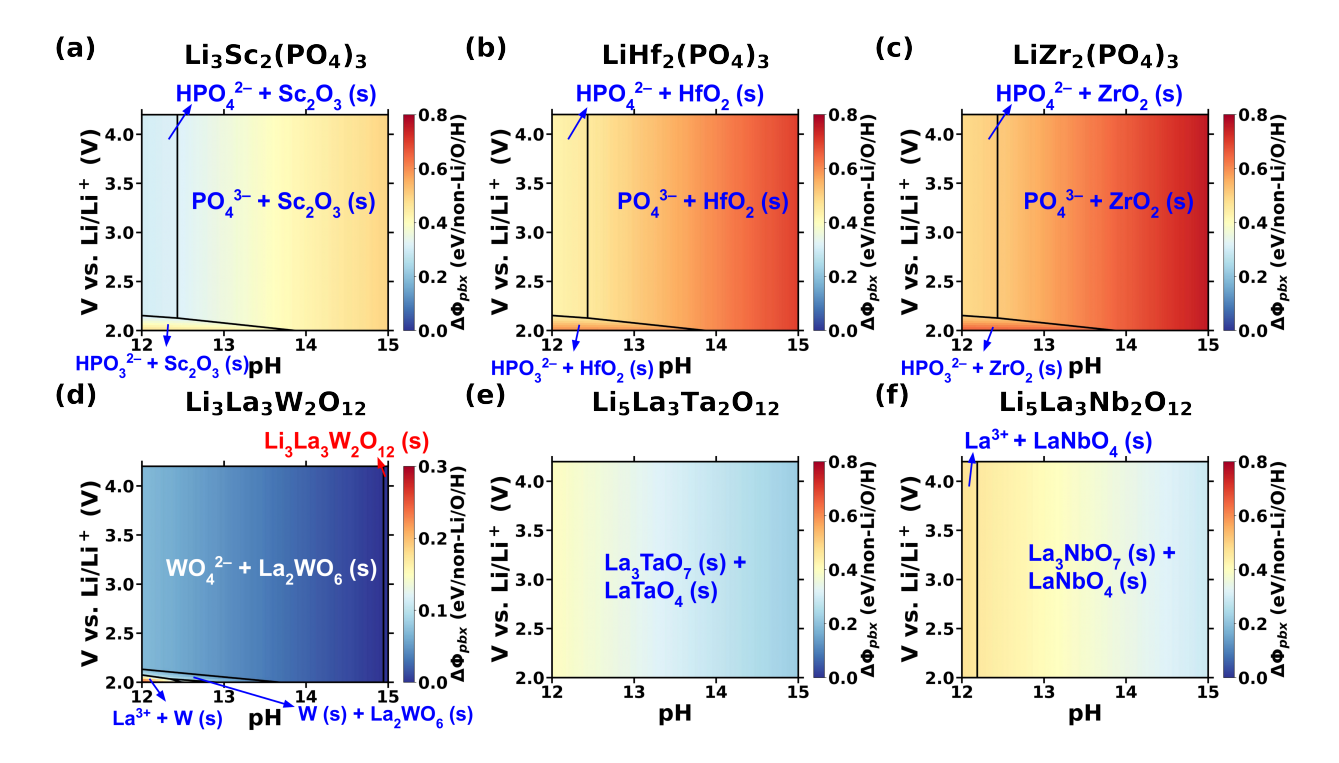


FIG. 8. Pourbaix diagrams of alkaline stable Li-ion conductors (a-c) NASICON, (d-f) garnet. The Pourbaix diagrams are constructed with DFT energies, following the correction scheme of Persson et. al. [44]. The color scheme shows the values of $\Delta\phi_{pbx}$ as a function of pH and V. The most stable decomposition products at different pH and V conditions are also labeled. Note that the color scheme in (d) is scaled differently from other plots for clarity purpose.

diagrams of some representative NASICON and garnet compounds substituted with cations identified as most beneficial to alkaline stability in Figure 7. The Pourbaix diagrams are obtained by using DFT-relaxed energies using the referencing approach developed by Persson et al [44]. The color scheme in the plots shows the variations of $\Delta \phi_{pbx}$ as a function of pH and voltage. The most stable decomposition products (either solid or ionic solution species) at different pH and voltage conditions are labeled in each Pourbaix diagram.

We first discuss the results for NASICON compounds. As shown in Figures 8 (a-c), $\text{Li}_3\text{Sc}_2(\text{PO}_4)_3$ exhibits lower $\Delta\phi_{pbx}$ compared to $\text{LiHf}_2(\text{PO}_4)_3$ and $\text{LiZr}_2(\text{PO}_4)_3$ and is thus likely to be more stable. This agrees with the results shown in Figure 7 (a) that Sc-based NASICON compounds in general have a lower max $\Delta\phi_{pbx}$ than Hf-based and Zr-based NASICONs. The Pourbaix diagram also suggests that all three NASICON compounds

exhibit higher values of $\Delta \phi_{pbx}$ as pH increases.

The decomposition products in the Pourbaix diagrams show that the dissolution of the PO_4^{3-} group drives the instability, leaving behind a solid TM oxide, mostly a binary oxide, at high pH conditions. The stability of the oxide decomposition is the reason why early TMs have the highest elemental PI of 1.0 (Figure 4 (e)). It was recently experimentally demonstrated that the dissolution of phosphate group is indeed the major cause of the degradation of phosphate-based NASICON compounds in alkaline solutions [62, 74]. We expect similar behavior from other types of polyanion groups, as the center cations in the polyanion groups, i.e., Si, S, V, and Mo, consistently exhibit low elemental PI values below 0.1, indicating their natural tendency to dissolve as ionic solution species at high pH conditions. Since none of these NASICON compounds are strictly stable, as indicated by the positive values of $\Delta \phi_{pbx}$, the bulk material can only be stabilized by surface passivation enabled by well-selected cation dopants in the octahedral sites.

In contrast, all garnet compounds considered in our screening contain lanthanum, which has a high elemental PI value of 0.84 (3 (e)), implying that all of these La-based garnet compounds should potentially form La-oxide-based surface passivation upon decomposition, irrespective of the cations occupying the octahedral site. To examine this hypothesis, we constructed Pourbaix diagrams for W-, Ta-, and Nb-based garnets (Li₃La₃W₂O₁₂, Li₅La₃Ta₂O₁₂, and Li₅La₃Nb₂O₁₂) as shown in Figures 8 (d-f). The hypothesis of La-based passivation is found to be mostly true, in a sense that all garnet compounds indeed decompose into La-based solid products for most of the pH and voltage ranges. However, instead of forming pure La-based binary oxides or hydroxides, all garnet compounds appear to decompose into La-M-O ternary oxides, where M is either W, Ta, or Nb. For example, the predominant solid products for Li₃La₃W₂O₁₂ is La₂WO₆, while it is the combination of LaTaO₄ and La₃TaO₇

and the combination of LaNbO₄ and La₃NbO₇ for Li₅La₃Ta₂O₁₂ and Li₅La₃Nb₂O₁₂, respectively. Similar results are obtained for Mo- and Sb-based garnets, which are predicted to form La₂MoO₆, and the combination of LaSbO₄ and La₃SbO₇, respectively, as the predominant solid products at high pH conditions (see Supplemental Information Figure S5). Furthermore, Figure 8 (d) also indicates that at the highest considered pH conditions (pH \approx 15), the garnet compound Li₃La₃W₂O₁₂ is predicted to remain intact without any decomposition. Our results indicate that an effective solid passivation is easier to be achieved for garnets than for NASICONs.

The substitutional metals (i.e., W, Ta, Nb, Mo, and Sb) that enhance garnet stability under alkaline conditions tend to have higher oxidation states (5+ or 6+) compared to Zr⁴⁺ in the baseline compound Li₇La₃Zr₂O₁₂. Consequently, garnets exhibiting a lower driving force to decompose in alkaline solutions $(\Delta \phi_{pbx})$ tend to have a lower Li content per formula unit (3 or 5 Li per 12 O). This raises the question of whether the reduced decomposition driving force originates primarily from the cation chemistry or from the lower Li content. As shown later in Figure 10 (c), the $\Delta \phi_{pbx}$ value indeed increases with Li content in garnet compounds. Although these two factors cannot be completely decoupled, our calculation indicate that low Li-content alone does not guarantee a low $\Delta \phi_{pbx}$ value. For example, CHGNet-predicted maximum $\Delta \phi_{pbx}$ values for Li₃La₃Te₂O₁₂, Li₃La₃Cr₂O₁₂ and Li₅La₃V₂O₁₂ garnet compounds are 1.84, 1.41 and 1.13 eV/non-Li/O/H, respectively, all exceeding the screening cutoff value (see Table IV in Methods). Moreover, Figure 7 shows that Te-, Cr-, V-substituted garnets are generally less stable under alkaline conditions. Overall, these results suggest that cation chemistry plays a more dominant role than Li content in governing the alkaline stability of garnet compounds.

The driving force for reaction in the highly alkaline environment $(\Delta \phi_{pbx})$ is substantially

lower for garnets than for NASICONs. It can also be observed that $\Delta \phi_{pbx}$ of these garnets even slightly decrease as pH increases, exhibiting an opposite trend to that of the NASICON compounds. This indicates that these garnet compounds might also be intrinsically more stable than the NASICONs even without surface passivation.

The variation of $\Delta \phi_{pbx}$ with pH can be rationalized by considering the change in the number of oxygen per chemical formula unit during decomposition. The grand Pourbaix potential ϕ_{pbx} can be mathematically expressed as (see Method section for the derivation)

$$\phi_{pbx} = G - N_O \cdot \mu_{H_2O} - (2N_O - N_H) \cdot RT \cdot \ln 10 \cdot \text{pH}$$
$$- N_{Li} \cdot \mu_{Li^+} - [(2N_O - N_H - N_{Li}) \cdot e + Q] \cdot V \tag{1}$$

where G is the Gibbs free energy of a given phase, N_O , N_H , and N_{Li} are the number of oxygen, hydrogen, and lithium in the compound, respectively, μ_{H_2O} is the chemical potential of a water molecule, and μ_{Li^+} is the Gibbs free energy of Li⁺ ion in the water, R is the gas constant, T is the temperature, e is the elemental charge, and Q is the charge for the ionic species. Since the grand Pourbaix potential ϕ_{pbx} varies linearly with $-N_O \cdot \text{pH}$, the grand Pourbaix decomposition energy $\Delta \phi_{pbx}$ also changes linearly with $-(N_{O,reactant} - N_{O,product}) \cdot \text{pH} = -\Delta N_O \cdot \text{pH}$, where the subscript "reactant" denotes either NASICON or garnet compound, the subscript "product" refers to the most stable decomposition products at a given pH and voltage condition. Because the decomposition of NASICONs results in the formation of a soluble phosphate group (PO₄³⁻) and a solid TM oxide (Sc₂O₃, HfO₂, or ZrO₂) at pH > 12.5 and most voltage values, the decomposition reaction absorbs additional oxygen from the environment. Take Li₃Sc₂(PO₄)₃ as an example (Figure 8 (a)), the decomposition reaction is Li₃Sc₂(PO₄)₃ \rightarrow 3Li⁺ + Sc₂O₃ + 3PO₄³⁻, and thus $\Delta N_O = -3$ per formula unit

of Li₃Sc₂(PO₄)₃. The negative sign of ΔN_O results in the $\Delta \phi_{pbx}$ values becoming more positive and the NASICON compounds being less stable as pH increases. In contrast, the primary decomposition products of garnets under most pH and voltage conditions are La-M-O ternary oxides (M = W, Ta, or Nb). The formation of ternary oxides results in the extraction of all lithium and the release of redundant oxygen upon decomposition, leading to positive values of ΔN_O . It should be noted that the formation of WO₄²⁻ in the decomposition of Li₃La₃W₂O₁₂ actually consumes additional oxygen, similar to the formation of TM binary oxides for NASICONs. However, in this case, $\Delta N_O = 1$ per formula unit of Li₃La₃W₂O₁₂ due to the following decomposition reaction: Li₃La₃W₂O₁₂ \rightarrow 3Li⁺ +0.5WO₄²⁻ +1.5La₂WO₆. Consequently, ΔN_O remains positive for all of these garnet compounds, making them more stable as pH increases. Such variation in $\Delta \phi_{pbx}$ with pH explains the trend observed across the majority of pH and voltage ranges depicted in Figure 8.

In summary, our results suggest that garnets not only have higher passivation capability, but also have lower driving force for dissolution in an alkaline solution than NASICONS, showing their superior potential as Li-ion conductors in high alkalinity.

D. Effect of polyanion group substitutions in NASICONs on alkaline stability

As can be seen from Figure 6 and Table I, there are many silicophosphate NASICONs in the final candidate list. To better understand how the stability of NASICON depends on the type of polyanion group, in Figure 9 we show the distributions of stability metrics for NASICON compounds that contain different polyanion groups. Compounds with mixed polyanion groups are excluded to allow for a direct comparison of individual polyanion types.

Among the nonmetal cation-based polyanion groups, i.e., silicates $((SiO_4)^{4-})$, phosphates $((PO_4)^{3-})$, and sulfates $((SO_4)^{2-})$, both V_{ox} and V_{red} decrease in the order of $(SO_4)^{2-} > (PO_4)^{3-}$

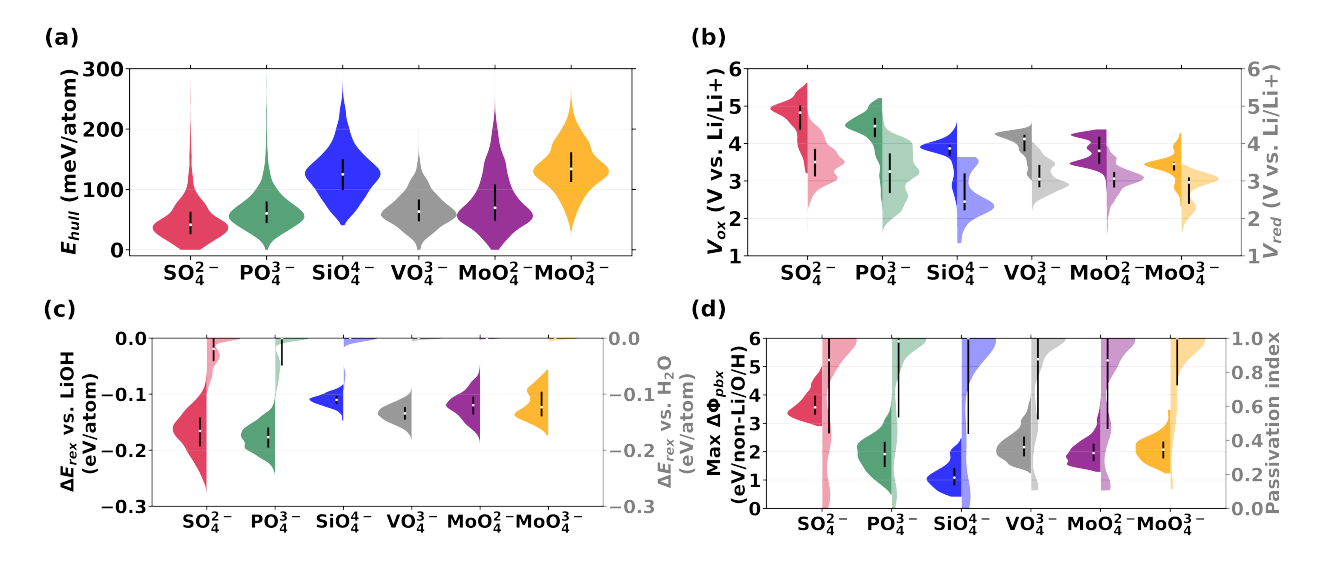


FIG. 9. Effect of polyanion group on the stability of NASICON (a) E_{hull} , (b) electrochemical stability, (c) chemical stability, and (d) alkaline stability. All stability metrics are based on CHGNet-relaxed energies. No compounds with mixed-polyanion groups are included. For the stability metrics other than E_{hull} , we only selected compounds with CHGNet-relaxed $E_{hull} < 100$ meV/atom to evaluate the trend within a set of reasonably stable compounds.

 $> ((\mathrm{SiO_4})^{4-}, \mathrm{a} \mathrm{\ trend} \mathrm{\ previously} \mathrm{\ attributed} \mathrm{\ to} \mathrm{\ the} \mathrm{\ inductive} \mathrm{\ effect} [61].$ The NASICONs with $(\mathrm{SiO_4})^{4-}$ groups tend to exhibit lower ΔE_{rex} against the reaction with LiOH compared to $(\mathrm{SO_4})^{2-}$ and $(\mathrm{PO_4})^{3-}$. In terms of the alkaline stability, there is a clear decreasing trend in max $\Delta \phi_{pbx}$ following the order of $(\mathrm{SO_4})^{2-} > (\mathrm{PO_4})^{3-} > ((\mathrm{SiO_4})^{4-}, \mathrm{making} \mathrm{\ silicates} \mathrm{\ the} \mathrm{\ most} \mathrm{\ stable}$ under high pH conditions. However, the pure silicate-based NASICON compounds may be more challenging to synthesize due to their higher E_{hull} compared to other compounds with different polyanions. This is also reflected in the subset of final candidates listed in Table I and in Supplemental Information. Although there are many silicophosphtates, none of the pure silicate-based NASICON compounds passed the final stage of screening.

For the polyanion groups with a TM center, both $(VO_4)^{3-}$ and $(MoO_4)^{2-}$ offer similar electrochemical and chemical stabilities as silicates, while exhibiting even lower E_{hull} . $(MoO_4)^{3-}$ compounds also demonstrate comparable electrochemical and chemical stabilities to $(VO_4)^{3-}$ and $(MoO_4)^{2-}$, but may be less synthesizable due to their higher E_{hull} . That said, all of these

vanadates and molybdates have higher max $\Delta \phi_{pbx}$ values than the silicates and some of the best phosphates. Our screening prioritize the compounds with higher alkaline stability. As a result, no molybdate-based and only few vanadate-substituted NASICONs remained in the final candidate list.

E. Li conductivity vs. alkaline stability

For the compounds listed in Tables I and II, the room-temperature Li-ion conductivities are evaluated by performing MD simulations using the fine-tuned CHGNet model (see the Methods section for the details on fine-tuning). More specifically, we run 1.4 ns-long MD simulations at high temperatures (500-1000 K), from which the Nernst-Einstein Li-ion conductivity at 300 K is extrapolated by assuming an Arrhenius relationship. For each MIEC compound, Li-ion conductivity is evaluated only for the composition that meets all DFT-screening criteria and has a Li content (x) closest to 1.5 for NASICON compounds and 7.0 for garnet compounds. These Li contents were experimentally shown to result in higher Li-ion conductivities [1, 2]. The CHGNet-predicted 300 K Li-ion conductivity and activation energy are plotted as a function of Li content in Figures 10 (a) and (b).

Figure 10 (a) shows that, consistent with experiments, NASICON compounds with Li content x = 1.5 achieve the highest room-temperature Li-ion conductivity. The high Li-ion conductivity is maintained for x = 2.0 or 2.5, whereas the compounds at two end-point compositions with x = 1.0 or 3.0 have much lower conductivity. The activation energy shows a similar trend, with E_a below 0.35 eV at $1.5 \le x \le 2.5$, while activation energies exceed 0.5 eV for x = 1.0 or 3.0 (see Figure 10 (b)). For garnet compounds, our simulation results agree with the experimental trend that the Li-ion conductivity generally increases with increasing Li content [1].

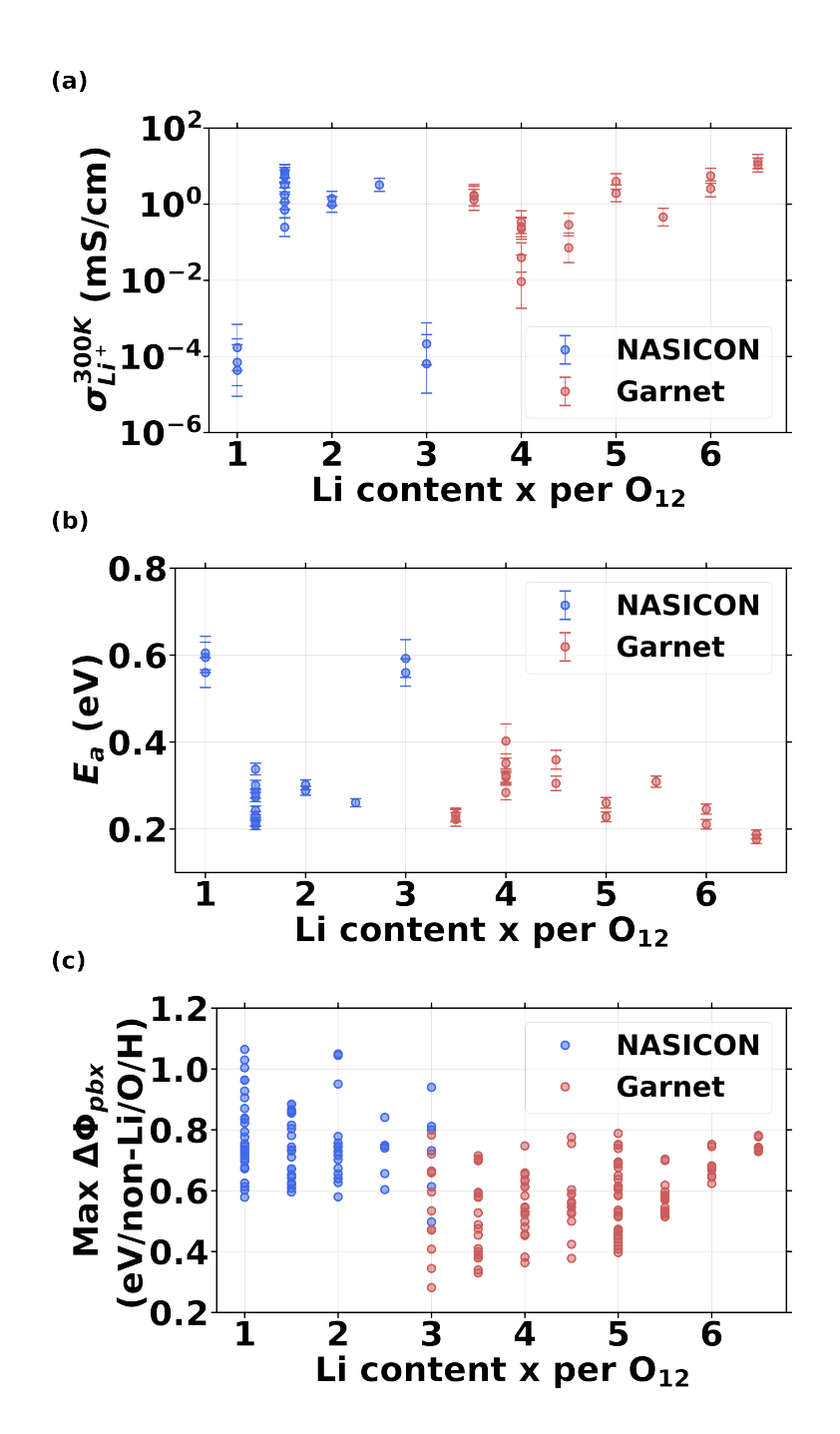


FIG. 10. Effect of Li content on the Nernst-Einstein Li-ion conductivity and alkaline stability (a) Li-ion conductivity at 300 K ($\sigma_{\text{Li}^+}^{300K}$) is extrapolated from the high-temperature conductivity obtained by fine-tuned CHGNet MD simulations at high temperature (500-1000 K). (b) Activation energy (E_a) of Li+ self diffusion coefficient, (c) max $\Delta \phi_{pbx}$ of all final SSE candidates (74 NASICON SSEs and 121 garnet SSEs) are plotted as a function of Li content. MIECs are excluded from the plots because the Li content of a MIEC varies as a function of applied voltage. The values of max $\Delta \phi_{pbx}$ are obtained from DFT-relaxed energies

To investigate if both high Li-ion conductivity and high alkaline stability can be achieved in the same composition, we plot in Figure 10 (c) max $\Delta\phi_{pbx}$ of all final SSE candidates (74 NASICON SSEs and 121 garnet SSEs), including the compounds considered in Figures 10 (a) and (b), as a function of Li content. The results show different trends between NASICON and garnet compounds: the NASICON compounds do not exhibit a clear dependence of max $\Delta\phi_{pbx}$ on the Li content, while the lowest max $\Delta\phi_{pbx}$ value increases with Li content for the garnet compounds. Our results suggest that for NASICON compounds, the Liion conductivity can potentially be optimized by tuning Li content without sacrificing the alkaline stability. However, for garnet compounds, Li stuffing increases Li-ion conductivity at the expense of the alkaline stability. As the improved alkaline stability of garnets with lower Li content is associated with the incorporation of specific high-valent transition metal cations (i.e., W⁶⁺, Ta⁵⁺, and Nb⁵⁺), careful compositional optimization is required to identify the sweet spot where garnet compounds can achieve both high Li-ion conductivity and robust alkaline stability.

F. Electronic conductivity vs. alkaline stability

The results shown in Figure 7 reveals that the first-row TMs, such as V, Cr, Mn, Fe, Co, and Ni, generally lead to high max $\Delta\phi_{pbx}$ values in both NASICON and garnet compounds, indicating that redox-active cations may destabilize the Li-ion conductors at high pH conditions. In Figure S6, we show the correlation between the amount of mixed-valent TMs in the NASICON or garnet compound and max $\Delta\phi_{pbx}$ values. The result indeed shows that max $\Delta\phi_{pbx}$ value increases by a factor of 2-3 as more mixed-valent TM cations are substituted (y decreases). Limiting the amount of TM may be a strategy to stabilize NASICON or garnet compounds, but to achieve good electronic conductivity, a high enough concentration

of redox-active metals along which polarons can hop has to be maintained [70, 75]. This suggests that achieving both high electronic conductivity and high alkaline stability may be intrinsically challenging. As we prioritize the compounds with higher alkaline stability in our screening, we obtained much more SSE (195 SSEs) compared to MIECs (14 MIECs) in the final candidate list. Also, the selected MIEC compounds have relatively low concentrations of the redox-active TMs.

IV. DISCUSSION

Oxide-based solid-state Li-ion conductors, especially NASICON and garnet-type conductors, have been widely studied for decades, and their crystal structures [76–81], Li-ion conduction mechanism [1, 2, 58], as well as electrochemical properties [10] are relatively well understood. Some of our large-scale screening results align with this general understanding. For example, our results indicate that the NASICON compounds are electrochemically more stable to higher voltage than the garnet compounds, which can be attributed to the inductive effect of the polyanion groups [61]. The goal of this work is to investigate the extent to which multiple key requirements for solid-state conductors can be optimized simultaneously. In particular, we focused on the trade-off between synthesizability, electrochemical stability, ionic conductivity, and stability in humid and alkaline environment. While these factors are broadly relevant to solid electrolytes, they are especially critical for solid-state humid Li-O₂ batteries. By leveraging the pretrained universal machine-learning interatomic potentials, we were able to cover a vast chemical space and understand the broad trade-offs between properties in them. We also successfully identified multiple NASICON and garnet compounds with properties that are superior to than their prototype compounds LiTi₂(PO₄)₃ and Li₇La₃Zr₂O₁₂ (see Figure 5). Moreover, our analysis points out the distinct advantages and disadvantages for each type of crystal framework, as summarized below.

Our results on the chemical reaction energies indicate that most of the NASICON compounds are quite resistive to moisture with negligible driving force to react with H_2O (Δ $E_{rex} \approx 0$ eV/atom, see Figure 5 (d)). This is consistent with the good water stability of NASICON compounds experimentally reported, where NASICON materials remained intact after being immersed in distilled water for 8 months [82]. In contrast, the garnet compounds are found to have a moderate reactivity with H_2O with Δ $E_{rex} < -0.1$ eV/atom (see Figure 5 (g))). It should be noted that we did not explicitly evaluate the materials stability with respect to a Li^+/H^+ exchange reaction, which is known to be an issue for garnet compounds used in a humid environment [15–17, 83]. This has been studied in detail in our separate publication [84].

As for the stability stability against reaction and dissolution in a highly alkaline medium (Figures 5 (e) and (h)), we found that both NASICON and garnet compounds exhibit positive max $\Delta\phi_{pbx}$ values, indicating that none of these compounds are strictly stable in a high pH solution. That said, our calculations also show that elemental substitution may substantially improve the alkaline stability (see Figures 7 and 9) either by decreasing the driving force for decomposition or by enabling the formation of a solid passivation layer through addition of elements that have good stability at high pH. For NASICON compounds, early transition metals such as Sc, Hf, and Zr are the most effective in enhancing alkaline stability, whereas W, Ta, and Nb are beneficial for improving the alkaline stability of garnet compounds. For garnet compounds, this means that alkaline-stable conductors typically have lower Li content, as they need to incorporate metals with high oxidation states (5+ or 6+). As a result, they tend to exhibit lower Li-ion conductivities, reflecting a trade-off between alkaline stability and conductivity.

A previous study revealed that the dissolution of NASICON in alkaline environment is largely driven by the dissolution of the polyanion groups [62, 74]. We suggest that replacing the phosphate by silicate groups is effective in decreasing the decomposition driving force. However, our calculations also predict that silicate-based lithium NASICONs may be more challenging to synthesize due to their generally higher energies above the convex hull, indicating a potential trade-off between the alkaline stability and the synthesizability. Mixing phosphate and silicate groups is a widely adopted strategy in sodium NASICON $Na_{1+x}Zr_2Si_xP_{3-x}O_{12}$ to reduce the Na-ion migration barrier [85, 86]. Some recent work indicates that the use of silicate groups can also increase the Li-ion diffusivity in lithium NASICONs [87, 88], but its effect effect on stability has been less explored [89]. In contrast, garnets lack polyanion groups in their structures, leading to much smaller predicted decomposition energies in alkaline solutions ($\Delta \phi_{pbx}$) than for NASICONs. Although Li stuffing in garnets increases the driving force to decompose in alkaline solutions, we identified many high Li-content garnet compounds with $\Delta\phi_{pbx}$ values that are comparable to those of the most alkaline-stable NASICONs. (see Figure 10 (c)). Therefore, we conclude that from both passivation and intrinsic stability perspectives, a garnet framework should exhibit a higher stability in alkaline conditions than a NASICON framework, though Li⁺/H⁺ exchange needs to be considered [16, 83, 84].

Our results (Figure S6) suggest that both NASICON and garnet compounds may face the same trade-off when trying to achieve high stability in alkaline conditions while retaining reasonable electronic conductivity, which may be particularly problematic when developing mixed conductors exposed to alkaline environments. This is because electronic conductivity requires some amount of redox-active cations. The exact amount of redox-active TM substitution required to achieve satisfactory electronic conductivity cannot be easily estimated,

as direct evaluation of electronic conductivity (such as the evaluation of polaron formation energy and migration energy using ab-initio methods [90]) is not conducted in our screening procedure and does not always provide quantitatively accurate information. A previous experimental study indicated that an increased electronic conductivity is achieved for MIEC garnets substituted with mixed-valent transition metals, with the electronic conductivity ranging from 10^{-5} to 10^{-6} S/cm [71]. In comparison, the electronic conductivity was only increased to $10^{-9}~\mathrm{S/cm}$ by lithiating initially electronically insulating $\mathrm{Li_{1.3}Al_{0.3}Ti_{1.7}(PO_4)_3}$ [72], which is still orders of magnitude lower than the Li-ion conductivity. The low electronic conductivity of NASICON compounds is believed to be intrinsic in nature due to the long polaron hopping distance originating from the vertex-sharing polyanion tetrahedra and metal octahedra which limit direct hopping between equivalent sites [61]. One of the highest experimentally reported electronic conductivity of 9×10^{-5} S/cm for NASI-CON is achieved by substituting V into the tetrahedral site of NASICON [91]. However, V-substitution in tetrahedral sites of a phosphate-based NASICON is found to reduce its alkaline stability in our screening (see Figure 9 (d)). As a result, only a few V-substituted NASICON compounds eventually passed the screening (see Figure 6 (a)). A more recent theoretical study pointed at Fe-substitution as effective in decreasing the polaron hopping barriers in lithium NASICON [70]. The elemental passivation index (PI) of Fe is quite high (0.81, see Figure 4), indicating that Fe-substitution may improve alkaline stability. We indeed obtained Fe-containing NASICON and garnet MIEC compounds (Li_xHf_{1.5}Fe_{0.5}(PO₄)₃ and $\rm Li_x La_3 Fe_{0.25} W_{1.75} O_{12})$ in the final candidate list. As experimental measurements of electronsections of the contract of tronic conductivities for redox-capable NASICONs are still rare, we call for more theoretical and experimental exploration to examine whether chemical substitutions alone is enough to achieve electronic conductivity comparable to its ionic counterpart.

V. CONCLUSION

In summary, we conducted a hierarchical high-throughput screening of possible alkaline-stable Li-ion conductors combining both machine-learning interatomic potentials (CHGNet model) and DFT calculations. We find that pretrained CHGNet model is effective in prescreening a vast range of chemistries, making it possible to chart almost the whole periodic table. We successfully identified 81 (74 SSEs and 7 MIECs) NASICON and 128 (121 SSEs and 7 MIECs) garnet compounds from over 300k and 6k initial NASICON and garnet candidates. Design principles for improving alkaline stability were derived from the screening, pointing out the effectiveness of specific cation substitutions, as well as the potential trade-offs among various materials properties. Our findings underscore the importance of multi-objective compositional optimization to balance competing properties, and suggests promising directions for the practical deployment of oxide-based Li-ion conductors, particularly in next-generation solid-state humid Li-O₂ batteries.

VI. METHODS

A. Substitution method

For the NASICON framework ($\text{Li}_{x}\text{M}_{2}(\text{AO}_{4})_{3}$), we used a hexagonal supercell with 72 O atoms, which has 12 octahedral sites in total. Up to 2 elements are allowed to substitute on octahedral sites, where the allowed substitution ratio include, 1/6, 1/4, 1/3, or 1/2. For garnet ($\text{Li}_{x}\text{La}_{3}\text{M}_{2}\text{O}_{12}$), we used the supercell size with 96 O atoms, which has 16 octahedral sites in total. Similar to NASICON, up to 2 elements are allowed to substitute on octahedral sites, where the allowed substitution ratio include, 1/8, 1/4, 3/8, or 1/2. For all NASICON and garnet compounds with different Li contents and cation substitutions, we first ordered

the Li/vacancy sites (6b. 36f, or 18e sites for NASICON; 24d or 96h for garnet), and then the cation substitution sites (M and A sites for NASICON; and M site only for garnet). The fractional occupation of Li ions in different Wycoff sites of NASICON are determined using two occupancy rules. The first rule involved populating lithium in 6b and 18e sites [79]: across all Li content range $(1 \le x \le 3)$, 6b sites are kept fully occupied, and the rest of Li occupies 18e sites. In the second rule, Li sequentially occupies 6b, 36f, and 18e sites as follows [76–78]: (1) For x = 1, all Li ions fully occupy 6b site. (2) For $1 < x \le 2$, Li in 6b sites are gradually replaced by Li in 36f sites, such that Li in 6b sites become vacant at x=2. (3) For $2 < x \le 3$, the fractional occupation of 36f is kept at 1/3, and the rest of Li occupies 18e sites. For each Li content and occupancy rule, we obtained 20 lowest electrostatic Ewald energy Li/vacancy configurations with a fixed cation ordering using pymatgen [92]. All the Li/vacancy configurations were relaxed using DFT calculations, from which the configuration with the lowest DFT-relaxed energy are selected. The fractional occupation of Li ions in different Wycoff sites of garnet are determined as follows [80, 81]: (1) For x=3, all Li ions fully occupy the 24d site. (2) For x = 7, half of the 24d sites are occupied, and the remaining Li ions occupy the 96h site . (3) For 3 < x < 7, the fractional occupancy in the 24d and 96h sites is linearly interpolated between the occupancy values at the two end-point Li contents. Similar to the case of NASICON, we chose Li/vacnacy configurations with the lowest DFT-relaxed energy among 20 low Ewald energy configurations. With the Li/vacancy configuration determined, we selected the ordering of substituted cations with the lowest Ewald energy. It should be noted that our ordering scheme does not guarantee the generation of thermodynamic ground state cation orderings, and thus all our energy values represent an upper bounds to those of the true ground state structures.

B. Electrochemical stability estimation

As explained in Subsection II C, the values of V_{ox} and V_{red} are calculated by including all topotactically related compositions. However, a slightly different procedures are applied in the CHGNet pre-screening step and the DFT screening step. During the CHGNet pre-screening step, we only included compounds whose E_{hull} values are below the cutoff value of 100 meV/atom. This excludes compounds that have relatively large driving force to decompose without any voltage applied. In the DFT screening step, if at least one topotactically related composition had an E_{hull} below the cutoff (25 meV/atom), making it synthesizable, the other topotactically related compounds with E_{hull} values exceeding the cutoff of 25 meV/atom were also included in the electrochemical stability analysis, assuming that all topotactically related compositions are kinetically accessible. In both screening steps, the values of V_{ox} and V_{red} can be higher and lower, respectively, than what one would obtain when only a single Li-content composition is considered.

C. Chemical stability estimation

The chemical reactivity is measured by the largest driving force (most negative ΔE_{rex}) of all possible reactions, considering different reactant ratios between the target NASICON or garnet compounds and the chemical species H₂O or LiOH. For compounds with mixed-valent TMs, the Li content within the compound can vary as voltage changes. In our screening, we used 2 separate schemes during the hierarchical 2-step screening. In the CHGNet prescreening step, all topotactically related compounds with different Li contents are considered to be stable, as long as one of them passes the screening criteria, given by a certain value of ΔE_{rex} above the cutoff. We call this the "inclusive scheme". In the DFT-screening step,

we applied a so-called "exclusive scheme", where all topotactically related compounds with varying Li contents are excluded from screening if any one of them does not meet the ΔE_{rex} screening criteria. In other words, we selected only those compounds that remain stable against H₂O or LiOH, regardless of their Li content.

D. Alkaline stability estimation

The alkaline stability is quantified by the grand Pourbaix potential, which is obtained by a Legendre transformation of Gibbs free energy G, [44, 45]

$$\phi_{pbx} = G - \mu_H \cdot N_H - \mu_O \cdot N_O - V \cdot Q - \mu_{Li} \cdot N_{Li} \tag{2}$$

where N_H , N_O , and N_{Li} are the number of hydrogen, oxygen, and lithium, respectively. μ_H , μ_O , and μ_{Li} are the chemical potential of hydrogen, oxygen, and lithium, respectively, V is the applied voltage, and Q is the net charge of a given phase. The above expression is identical to the conventional Pourbaix potential ψ_{pbx} , except for the last term $-\mu_{Li} \cdot N_{Li}$. This term arises from our assumption that the battery system is also open to lithium in addition to hydrogen, oxygen and electron during the battery operation.

Following the Pourbaix formalism developed by Persson et al.[44], the hydrogen chemical potential is corrected based on the liquid water (μ_{H_2O}) and gas phase O_2 energies ($\mu_{O_2} = 2\mu_O$), such that the computational formation energy of H_2O is aligned with its experimental Gibbs free energy as follows,

$$\mu_{H_2O} = \mu_O + 2\mu_H \tag{3}$$

In addition, the chemical potentials of hydrogen and lithium are both voltage dependent,

$$\mu_H = \mu_{H^+} - eV \tag{4}$$

$$\mu_{Li} = \mu_{Li^+} - eV \tag{5}$$

where $\mu_{H^+} = -RT \cdot \ln 10 \cdot \text{pH}$, and $\mu_{Li^+} = \mu_{Li^+}^0 + RT \cdot \ln[a_{Li^+}]$. Here, R is the gas constant, and T is the temperature. $\mu_{Li^+}^0$ is the standard-state Gibbs free energy of Li⁺ ion in the water, and a_{Li^+} is the activity of Li⁺. e is the elemental charge. T is set to 298 K and a_{Li^+} is set to 1.0 M throughout our screening. Equation (1) can be easily derived from Equations (2-5).

We use DFT-relaxed energy at 0 K as an approximation for G of all solid phases. The Gibbs free energies of all ionic phases are tabulated in pymatgen, which are also used in our study. The activity of all ionic solution species except Li⁺ are set to 10^{-6} M. We apply entropy correction to the gas phase (O_2) and liquid phase (H_2O) , as well as the energy correction to the ionic phases according to MaterialsProjectAqueousCompatibility implemented in pymatgen.

E. Screening criteria

In the Tables III and IV, we listed the cutoff values we used in the CHGNet pre-screening step and DFT-screening step for both NASICON and garnet compounds. Most of the stability metrics use the same or even stricter values in the DFT-screening step compared to those in the CHGNet pre-screening step. The exception is for V_{ox} , where a slightly lower cutoff values are set in DFT-screening step. This is because when we calculate the electrochemical stability in the DFT-screening step, we used a smaller shift value below

the convex hull for the metastable compounds (1 meV/atom for DFT-screening step, in comparison to 10 meV/atom for CHGNet pre-screening step), in order to be less inclusive than in the CHGNet pre-screening step. Consequently, a lower oxidation limit cutoff is necessary to pass a sufficient number of final candidate compounds.

TABLE III. Screening criteria for NASICON compounds

	CHGNet pre-screening step	DFT-screening step
E_{hull} (eV/atom)	< 0.1	< 0.025
ΔE_{rex} vs. H ₂ O (eV/atom)	> -0.15	> -0.15
ΔE_{rex} vs. LiOH (eV/atom)	> -0.15	> -0.15
V_{ox} (V vs. Li/Li ⁺)	> 4.2	> 4.0
V_{red} (V vs. Li/Li ⁺)	< 2.6	< 2.6
$\max_{\text{(eV/non-Li/O/H)}} \phi_{pbx}$	< 1.1	< 1.1
PI	> 0.8	> 0.8
Comment	 Inclusive scheme for chemical stability screening Shift 10 meV/atom below the convex hull for estimating Vox and Vred of metastable phases 	·

TABLE IV. Screening criteria for garnet compounds

	CHGNet pre-screening step	DFT-screening step
E_{hull} (eV/atom)	< 0.1	< 0.025
ΔE_{rex} vs. H ₂ O (eV/atom)	> -0.1	> -0.03
ΔE_{rex} vs. LiOH (eV/atom)	> -0.1	> -0.03
V_{ox} (V vs. Li/Li ⁺)	> 3.1	> 3.0
V_{red} (V vs. Li/Li ⁺)	< 2.0	< 2.0
$\max_{\text{(eV/non-Li/O/H)}} \phi_{pbx}$	< 1.1	< 0.8
PI	> 0.8	> 0.8
Comment	• Inclusive scheme for chemical stability screening	• Exclusive scheme for chemical stability screening
	• Shift 10 meV/atom below the convex hull for estimating V_{ox} and V_{red} of metastable phases	• Shift 1 meV/atom below the convex hull for estimating V_{ox} and V_{red} of metastable phases

F. DFT and CHGNet relaxations

DFT calculations were performed within the projector augmented wave (PAW) formalism [93], using the Vienna ab initio simulation package [94]. All DFT relaxations were performed using Perdew-Burke-Ernzerhof (PBE) generalized gradient approximation (GGA) functional[95] and converged to 10^{-5} eV for energy and 0.05 eV/Å for force respectively. In the CHGNet pre-screening step, we used pretrained CHGNet model [36]. All CHGNet relaxations were converged to 0.1 eV/Å for force.

It should be noted that the Li intercalation voltages predicted by DFT calculations within GGA usually underestimate the experimentally measured voltages[96]. The discrepancy in the voltage prediction can be reduced by using Hubbard+U method [97–99]. In our DFT calculations, the same +U values are applied to the TMs (3d: V, Cr, Mn, Fr, Ni, Co, 4d:

Mo, 5d: W) as the default values of MPRelaxSet implemented in pymatgen, where the U values are obtained by fitting to experimental binary formation enthalpies [100].

G. CHGNet fine-tuning and MD simulation

To run MD simulations for subsets of NASICON and garnet final candidates listed in Tables I and II, we fine-tuned two CHGNet models separately for NASICON and garnet compounds, similar to a previous workflow [56]. The dataset is constructed by running MD simulations using pretrained CHGNet model, followed by DFT static calculations on selected MD trajectory frames. The MD simulations with pretrained CHGNet model are performed for all compounds listed in Tables I and II for a duration of 0.5 ns at multiple temperatures (500 K, 600 K, 700 K, 800 K, 900 K, and 1000 K) with a time-step of 2 fs. We uniformly chose 100 trajectory frames for each MD simulation run, resulting in 10,200 frames and 10,800 frames for NASICON and garnet, respectively. The DFT static calculations for these selected frames are performed with the electronic convergence criteria of 10⁻⁵ eV using DFT settings compatible with the Materials Project database.

The fine-tuning for garnet CHGNet model is performed by tuning all atom, bond, and angle convolution layers, while keeping all other layers freezed. On the other hand, we found that the same fine-tuning scheme results in unphysical crystal configurations for the NASICON model during the MD simulations. For instance, some tetrahedral PO₄ polyanion groups became trigonal plane PO₃ groups with one broken P-O bond during those MD simulations. Therefore, the fine-tuning for NASICON CHGNet model was performed by freezing all layers, except only the last layers of atom, bond, and angle convolution layers. Both NASICON and garnet CHGNet models are fine-tuned with a 0.9:0.05:0.05 ratio for training, validation, and test datasets. The fine-tuning was conducted up to 100 epochs,

and the models with the lowest force error were picked as the optimal models. The energy and force errors of the fine-tuned models are 0 meV and 47 meV/Å for NASICON, and for 2 meV and 37 meV/Å for garnet models.

MD simulations with fine-tuned CHGNet models were performed at various temperatures (500 K, 600 K, 700 K, 800 K, 900 K, and 1000 K). The MD systems were initially heated up to the target temperatures in 2 ps using Berendsen thermodstat, followed by 100 ps of equilibration using Nosé–Hoover thermostat. The ionic trajectories are sampled in the final 1.4-ns production stage using Nosé–Hoover thermostat. All MD simulations were performed in NVT ensemble with a time step of 2 fs. Li-ion conductivity at 300 K and activation energy are obtained by extrapolating from the high-temperature conductivities assuming the Arrhenius relationship. The error error bounds (upper and lower limits) of Li-ion conductivity and the standard deviation of activation energy were evaluated using the scheme previously established [65].

VII. AUTHOR CONTRIBUTIONS

Z.L and K.J. contributed equally to this work. Z.L and K.J. designed the screening procedures, and conducted all calculations. B.D. contributed to the fine-tuning of CHGNet models. The manuscript was written by Z.L. and K.J., and revised by B.D. and G.C. The work was supervised by G.C.

VIII. ACKNOWLEDGMENT

This work was supported by the Samsung Advanced Institute of Technology (SAIT).

This research used computational resources of the National Renewable Energy Laboratory

(NREL) clusters under the *saepssic* allocation. K.J. acknowledges support from Kwanjeong Educational Foundation Scholarship.

IX. SUPPLEMENTAL INFORMATION

The Supplemental material is available at URL-When-Published.

[1] Venkataraman Thangadurai, Sumaletha Narayanan, and Dana Pinzaru. Garnet-type solid-state fast Li ion conductors for Li batteries: critical review. *Chem Soc Rev*, 43:4714–4727, 2014.

- [2] Andreas Rossbach, Frank Tietz, and Steffen Grieshammer. Structural and transport properties of lithium-conducting NASICON materials. *Journal of Power Sources*, 391(January):1–9, 2018.
- [3] S Stramare, V Thangadurai, and W Weppner. Lithium Lanthanum Titanates: A Review. *Chemistry of Materials*, 15:3974–3990, 2003.
- [4] Jaegyeom Kim, a Juhyun Kim, a Maxim Avdeev, Hoseop Yun, and Seung-Joo Kim. A fast lithium-ion conductor with new framework structure. *Journal of Materials Chemistry A*, 4:22478–22482, 2018.
- [5] Laidong Zhou, Nicolò Minafra, Wolfgang G. Zeier, and Linda F. Nazar. Innovative Approaches to Li-Argyrodite Solid Electrolytes for All-Solid-State Lithium Batteries. *Accounts of Chemical Research*, 54(12):2717–2728, 2021.
- [6] Boran Tao, Chaojun Ren, Hongda Li, Baosheng Liu, Xiaobo Jia, Xinwei Dong, Shaohui Zhang, and Haixin Chang. Thio-/LISICON and LGPS-Type Solid Electrolytes for All-Solid-State Lithium-Ion Batteries. *Advanced Functional Materials*, 32(34):1–25, 2022.
- [7] Takuya Kimura, Takeaki Inaoka, Ryo Izawa, Takumi Nakano, Chie Hotehama, Atsushi Sakuda, Masahiro Tatsumisago, and Akitoshi Hayashi. Stabilizing High-Temperature α -Li3PS4 by Rapidly Heating the Glass. *Journal of the American Chemical Society*, 145(26):14466–14474, 2023.
- [8] Changhong Wang, Jianwen Liang, Jung Tae Kim, and Xueliang Sun. Prospects of halide-based all-solid-state batteries: From material design to practical application. *Science Advances*, 8:eadcv9516, 2022.
- [9] Hiram Kwak, Shuo Wang, Juhyoun Park, Yunsheng Liu, Kyu Tae Kim, Yeji Choi, Yifei Mo, and Yoon Seok Jung. Emerging Halide Superionic Conductors for All-Solid-State Batteries: Design, Synthesis, and Practical Applications. *ACS Energy Letters*, 7(5):1776–1805, 2022.
- [10] William D. Richards, Lincoln J. Miara, Yan Wang, Jae Chul Kim, and Gerbrand Ceder. Interface Stability in Solid-State Batteries. *Chemistry of Materials*, 28(1):266–273, 2016.
- [11] Yizhou Zhu, Xingfeng He, and Yifei Mo. First principles study on electrochemical and chemical stability of solid electrolyte-electrode interfaces in all-solid-state Li-ion batteries. *Journal of Materials Chemistry A*, 4(9):3253–3266, 2016.

- [12] Yihan Xiao, Yan Wang, Shou Hang Bo, Jae Chul Kim, Lincoln J. Miara, and Gerbrand Ceder. Understanding interface stability in solid-state batteries. *Nature Reviews Materials*, 5(2):105–126, 2020.
- [13] Hiromasa Muramatsu, Akitoshi Hayashi, Takamasa Ohtomo, Sigenori Hama, and Masahiro Tatsumisago. Structural change of Li2S-P2S5 sulfide solid electrolytes in the atmosphere. *Solid State Ionics*, 182(1):116–119, 2011.
- [14] Renfei Feng, Ruying Li, Li Zhang, Shigang Lu, Huan Huang, Shangqian Zhao, and Tsunkong Sham. Unraveling the Origin of Moisture Stability of Halide Solid-State Electrolytes by In Situ and Operando Synchrotron X ray Analytical Techniques. *Chemistry of Materials*, 23:7019–7027, 2020.
- [15] Lei Cheng, Miao Liu, Apurva Mehta, Huolin Xin, Feng Lin, Kristin Persson, Guoying Chen, Ethan J. Crumlin, and Marca Doeff. Garnet Electrolyte Surface Degradation and Recovery. ACS Applied Energy Materials, 1(12):7244-7252, 2018.
- [16] Ruijie Ye, Martin Ihrig, Nobuyuki Imanishi, Martin Finsterbusch, and Egbert Figgemeier. A Review on Li+/H+ Exchange in Garnet Solid Electrolytes: From Instability against Humidity to Sustainable Processing in Water. ChemSusChem, 14(20):4397–4407, 2021.
- [17] Asma Sharafi, Seungho Yu, Michael Naguib, Marcus Lee, Cheng Ma, Harry M. Meyer, Jagjit Nanda, Maiofang Chi, Donald J. Siegel, and Jeff Sakamoto. Impact of air exposure and surface chemistry on Li-Li7La3Zr2O12 interfacial resistance. *Journal of Materials Chemistry* A, 5(26):13475–13487, 2017.
- [18] Panpan Xu, Xingyu Guo, Binglei Jiao, Jinxing Chen, Minghao Zhang, Haodong Liu, Xiaolu Yu, Maura Appleberry, Zhenzhen Yang, Hongpeng Gao, Fan Yang, Xuefei Weng, Yanbin Shen, Jing Gu, Ying Shirley Meng, Christopher Brooks, Shyue Ping Ong, and Zheng Chen. Proton-exchange induced reactivity in layered oxides for lithium-ion batteries. *Nature Communications*, 15(1), 2024.
- [19] Lianfeng Zou, Yang He, Zhenyu Liu, Haiping Jia, Jian Zhu, Jianming Zheng, Guofeng Wang, Xiaolin Li, Jie Xiao, Jun Liu, Ji Guang Zhang, Guoying Chen, and Chongmin Wang. Unlocking the passivation nature of the cathode—air interfacial reactions in lithium ion batteries. *Nature Communications*, 11:3204, 2020.
- [20] Masato Takeuchi, Ryo Kurosawa, Junichi Ryu, and Masaya Matsuoka. Hydration of LiOH and LiCl-Near-Infrared Spectroscopic Analysis. *ACS Omega*, 6(48):33075–33084, 2021.
- [21] Christophe Monnin and Michel Dubois. Thermodynamics of the LiOH + H2O system. Journal of Chemical and Engineering Data, 50(4):1109–1113, 2005.
- [22] Hyunjin Kim, Hyunpyo Lee, Wonsung Choi, Gabin Yoon, Changhoon Jung, Mokwon Kim, Taeyoung Kim, Jung Park, and Dongmin Im. Operando Observation of the De-Evolution/Evolution Process of Hydrated LiOH in Moisture-Assisted Li-O 2 Batteries. ACS Applied Materials & Interfaces, 15(24):29120–29126, 2023.
- [23] Alan C Luntz and Bryan D Mccloskey. Nonaqueous Li-Air Batteries : A Status Report. Chemical Reviews, 114:11721—11750, 2014.
- [24] Zhuojian Liang, Wanwan Wang, and Yi Chun Lu. The path toward practical Li-air batteries. Joule, 6(11):2458–2473, 2022.
- [25] Tao Liu, J Padmanabhan Vivek, Evan Wenbo Zhao, Jiang Lei, Nuria Garcia-araez, and Clare P Grey. Current Challenges and Routes Forward for Nonaqueous Lithium Air Batteries. *Chemical Reviews*, 120:6558–6625, 2020.
- [26] Ziyang Guo, Xiaoli Dong, Shouyi Yuan, Yonggang Wang, and Yongyao Xia. Humidity effect on electrochemical performance of Li e O 2 batteries. *Journal of Power Sources*, 264:1–7,

- 2014.
- [27] Tao Liu, Michal Leskes, Wanjing Yu, Amy J Moore, Lina Zhou, Paul M Bayley, Gunwoo Kim, and Clare P Grey. Cycling Li-O2 batteries via LiOH formation and decomposition. Science, 350(6260):3–6, 2015.
- [28] P. Tan, W. Shyy, T. S. Zhao, R. H. Zhang, and X. B. Zhu. Effects of moist air on the cycling performance of non-aqueous lithium-air batteries. *Applied Energy*, 182:569–575, 2016.
- [29] Yun Guang Zhu, Qi Liu, Yangchun Rong, Haomin Chen, Jing Yang, Chuankun Jia, Li Juan Yu, Amir Karton, Yang Ren, Xiaoxiong Xu, Stefan Adams, and Qing Wang. Proton enhanced dynamic battery chemistry for aprotic lithium-oxygen batteries. *Nature Communications*, 8:4–11, 2017.
- [30] Zongyan Gao, Israel Temprano, Jiang Lei, Linbin Tang, Junjian Li, and Clare P Grey. Recent Progress in Developing a LiOH-Based Reversible Nonaqueous Lithium Air Battery. *Advanced Materials*, 35:2201384, 2023.
- [31] K Uta Schwenke, Michael Metzger, Tassilo Restle, Michele Piana, and Hubert A Gasteiger. The Influence of Water and Protons on Li 2 O 2 Crystal Growth in Aprotic Li-O 2 Cells The Influence of Water and Protons on Li 2 O 2 Crystal Growth in. *Journal of The Electrochemical Society*, 162(4):A573–A584, 2015.
- [32] Nagaphani B Aetukuri, Bryan D Mccloskey, Jeannette M García, Leslie E Krupp, Venkatasubramanian Viswanathan, and Alan C Luntz. Solvating additives drive solution-mediated electrochemistry and enhance toroid growth in non-aqueous Li – O 2 batteries. *Nature Chemistry*, 7(January), 2015.
- [33] Shunchao Ma, Jiawei Wang, Jun Huang, Zhen Zhou, and Zhangquan Peng. Unveiling the Complex E ff ects of H 2 O on Discharge Recharge Behaviors of Aprotic Lithium O 2 Batteries. The journal of physical chemistry lettersPhysical Chemistry Letters, 9:3333–3339, 2018.
- [34] Mokwon Kim, Hyunpyo Lee, Hyuk Jae Kwon, Seong-min Bak, Cherno Jaye, Daniel A Fischer, Gabin Yoon, Jung O Park, Dong-hwa Seo, Sang Bok Ma, and Dongmin Im. Carbon-free high-performance cathode for solid-state Li-O 2 battery. *Science Advances*, 2(April):1–10, 2022.
- [35] Fujun Li, Shichao Wu, De Li, Tao Zhang, Ping He, Atsuo Yamada, and Haoshen Zhou. The water catalysis at oxygen cathodes of lithium-oxygen cells. *Nature Communications*, 6:7843, 2015.
- [36] Bowen Deng, Peichen Zhong, KyuJung Jun, Janosh Riebesell, Kevin Han, Christopher J. Bartel, and Gerbrand Ceder. CHGNet: Pretrained universal neural network potential for charge-informed atomistic modeling. *Nature Machine Intelligence*, 5:1031–1041, 2023.
- [37] Bin Ouyang, Jingyang Wang, Tanjin He, Christopher J. Bartel, Haoyan Huo, Yan Wang, Valentina Lacivita, Haegyeom Kim, and Gerbrand Ceder. Synthetic accessibility and stability rules of NASICONs. *Nature Communications*, 12(1):1–11, 2021.
- [38] Wenhao Sun, Stephen T Dacek, Shyue Ping Ong, Geoffroy Hautier, Anubhav Jain, William D Richards, Anthony C Gamst, Kristin A Persson, and Gerbrand Ceder. The thermodynamic scale of inorganic crystalline metastability. *Science Advances*, 2:e1600225, 2016.
- [39] Muratahan Aykol, Shyam S Dwaraknath, Wenhao Sun, and Kristin A Persson. Thermodynamic limit for synthesis of metastable inorganic materials. Science Advances, 4:eaaq0148, 2018.
- [40] Yifei Mo, Shyue Ping Ong, and Gerbrand Ceder. First principles study of the Li 10GeP 2S 12 lithium super ionic conductor material. *Chemistry of Materials*, 24(1):15–17, 2012.

- [41] Yizhou Zhu, Xingfeng He, and Yifei Mo. Origin of Outstanding Stability in the Lithium Solid Electrolyte Materials: Insights from Thermodynamic Analyses Based on First-Principles Calculations. ACS Applied Materials and Interfaces, 7(42):23685–23693, 2015.
- [42] Kyu Jung Jun, Lori Kaufman, Wangmo Jung, Byungchun Park, Chiho Jo, Taegu Yoo, Donghun Lee, Byungju Lee, Bryan D. McCloskey, Haegyeom Kim, and Gerbrand Ceder. Understanding the Irreversible Reaction Pathway of the Sacrificial Cathode Additive Li6CoO4. Advanced Energy Materials, 13(30), 2023.
- [43] Nathan J Szymanski, Young-Woon Byeon, Yingzhi Sun, Yan Zeng, Jianming Bai, Martin Kunz, Min Kim, Brett A Helms, and Christopher J Bartel. Quantifying the regime of thermodynamic control for solid- state reactions during ternary metal oxide synthesis. Science Advances, 10:eadp3309, 2024.
- [44] Kristin A Persson, Bryn Waldwick, Predrag Lazic, and Gerbrand Ceder. Prediction of solid-aqueous equilibria: Scheme to combine first-principles calculations of solids with experimental aqueous states. *Physical Review B*, 85:235438, 2012.
- [45] Wenhao Sun, Daniil A Kitchaev, Denis Kramer, and Gerbrand Ceder. Non-equilibrium crystallization pathways of manganese oxides in aqueous solution. *Nature Communications*, 10(1):573, 2019.
- [46] Zheren Wang, Yingzhi Sun, Kevin Cruse, Yan Zeng, Yuxing Fei, Zexuan Liu, Junyi Shangguan, Young Woon Byeon, Kyu Jung Jun, Tanjin He, Wenhao Sun, and Gerbrand Ceder. Optimal thermodynamic conditions to minimize kinetic by-products in aqueous materials synthesis. *Nature Synthesis*, 3(4):527–536, 2024.
- [47] Arunima K Singh, Lan Zhou, Aniketa Shinde, Santosh K Suram, Joseph H Montoya, Donald Winston, John M Gregoire, and Kristin A Persson. Electrochemical Stability of Metastable Materials. *Chemistry of Materials*, 29:10159—10167, 2017.
- [48] Chunhua Xu and Wei Gao. Pilling-Bedworth ratio for oxidation of alloys. *Material Research Innovations*, 3:231–235, 2000.
- [49] Jürgen Barthel and Rainer Deiss. The limits of the Pourbaix diagram in the interpretation of the kinetics of corrosion and cathodic protection of underground pipelines. *Materials and Corrosion*, 72(3):434–445, 2021.
- [50] Zening Wang, Yu Yan, Yuan Wu, Yi Zhang, Xinpeng Zhao, Yanjing Su, and Lijie Qiao. Recent research progress on the passivation and selective oxidation for the 3d-transition-metal and refractory multi-principal element alloys. *npj Materials Degradation*, 7(1), 2023.
- [51] Lauren N. Walters, Liang Feng Huang, and James M. Rondinelli. First-Principles-Based Prediction of Electrochemical Oxidation and Corrosion of Copper under Multiple Environmental Factors. Journal of Physical Chemistry C, 125(25):14027–14038, 2021.
- [52] Chunhua Xu and Wei Gao. Pilling-Bedworth ratio for oxidation of alloys. *Material Research Innovations*, 3:231–235, 2000.
- [53] Digby Macdonald. Theory of Passive Film Stability. ECS Transactions, 2(9):73–81, 2007.
- [54] Anubhav Jain, Shyue Ping Ong, Geoffroy Hautier, Wei Chen, William Davidson Richards, Stephen Dacek, Shreyas Cholia, Dan Gunter, David Skinner, Gerbrand Ceder, Kristin A Persson, Anubhav Jain, Ping Ong, Geoffroy Hautier, Wei Chen, Dan Gunter, David Skinner, Gerbrand Ceder, and Kristin A Persson. Commentary: The Materials Project: A materials genome approach to accelerating materials innovation Commentary: The Materials Project: A materials genome. APL, 1:011002, 2018.
- [55] Matthew K Horton, Patrick Huck, Ruo Xi Yang, Jason M Munro, Shyam Dwaraknath, Alex M Ganose, Ryan S Kingsbury, Mingjian Wen, Jimmy X Shen, Tyler S Mathis, Aaron D

- Kaplan, Karlo Berket, Janosh Riebesell, Janine George, Andrew S Rosen, Evan W C Spottesmith, Matthew J Mcdermott, Orion A Cohen, Alex Dunn, Matthew C Kuner, Gian-marco Rignanese, Guido Petretto, David Waroquiers, Sinead M Griffin, Jeffrey B Neaton, Daryl C Chrzan, Mark Asta, Geoffroy Hautier, Shreyas Cholia, Gerbrand Ceder, Shyue Ping Ong, Anubhav Jain, and Kristin A Persson. Accelerated data-driven materials science with the Materials Project. *Nature Materials*, (Ml), 2025.
- [56] KyuJung Jun, Yihan Xiao, Wenhao Sun, Young-Woon Byeon, Haegyeom Kim, and Gerbrand Ceder. Nitride Lithium-ion Conductors with Enhanced Oxidative Stability. *Journal of The Electrochemical Society*, 2024.
- [57] Peichen Zhong, Sunny Gupta, Bowen Deng, Kyu Jung Jun, and Gerbrand Ceder. Effect of Cation Disorder on Lithium Transport in Halide Superionic Conductors. ACS Energy Letters, 9(6):2775–2781, 2024.
- [58] Yihan Xiao, Kyu Jung Jun, Yan Wang, Lincoln J. Miara, Qingsong Tu, and Gerbrand Ceder. Lithium Oxide Superionic Conductors Inspired by Garnet and NASICON Structures. *Advanced Energy Materials*, 11(37), 2021.
- [59] Wenhao Sun, Stephen T Dacek, Shyue Ping Ong, Geoffroy Hautier, Anubhav Jain, William D Richards, Anthony C Gamst, Kristin A Persson, and Gerbrand Ceder. The thermodynamic scale of inorganic crystalline metastability. *Science Advances*, 2:e1600225, 2016.
- [60] Fudong Han, Yizhou Zhu, Xingfeng He, Yifei Mo, and Chunsheng Wang. Electrochemical Stability of Li10GeP2S12 and Li7La3Zr2O12 Solid Electrolytes. *Advanced Energy Materials*, 6(8):1–9, 2016.
- [61] Christian Masquelier and Laurence Croguennec. Polyanionic (Phosphates, Silicates, Sulfates) Frameworks as Electrode Materials for Rechargeable Li (or Na) Batteries. *Chemical Reviews*, 113(8):6552–6591, aug 2013.
- [62] Benjamin X. Lam, Zhuohan Li, Tara P. Mishra, and Gerbrand Ceder. Degradation Mechanism of Phosphate-Based Li-NASICON Conductors in Alkaline Environment. Advanced Energy Materials, 2403596, 2024.
- [63] Satoshi Hasegawa, Nobuyuki Imanishi, Tao Zhang, Jian Xie, Atsushi Hirano, Yasuo Takeda, and Osamu Yamamoto. Study on lithium/air secondary batteries-Stability of NASICON-type lithium ion conducting glass-ceramics with water. *Journal of Power Sources*, 189(1):371–377, 2009.
- [64] Yuta Shimonishi, Tao Zhang, Nobuyuki Imanishi, Dongmin Im, Dong Joon Lee, Atsushi Hirano, Yasuo Takeda, Osamu Yamamoto, and Nigel Sammes. A study on lithium/air secondary batteries Stability of the NASICON-type lithium ion conducting solid electrolyte in alkaline aqueous solutions. *Journal of Power Sources*, 196(11):5128–5132, 2011.
- [65] Xingfeng He, Yizhou Zhu, Alexander Epstein, and Yifei Mo. Statistical variances of diffusional properties from ab initio molecular dynamics simulations. *npj Computational Materials*, 4(18), 2018.
- [66] A. Venkateswara Rao, V. Veeraiah, A. V. Prasada Rao, and B. Kishore Babu. Effect of Fe3+ doping on the structure and conductivity of LiTi2(PO4)3. Research on Chemical Intermediates, 41(4):2307–2315, 2015.
- [67] Miguel A. París, Ana Martínez-Juárez, José M. Rojo, and Jesús Sanz. Lithium mobility in the NASICON-type compound LiTi2(PO4)3 by nuclear magnetic resonance and impedance spectroscopies. *Journal of Physics Condensed Matter*, 8(29):5355–5366, 1996.
- [68] Yutao Li, Jian Tao Han, Chang An Wang, Sven C. Vogel, Hui Xie, Maowen Xu, and John B. Goodenough. Ionic distribution and conductivity in lithium garnet Li 7La 3Zr 2O 12. *Journal*

- of Power Sources, 209:278-281, 2012.
- [69] Cesare Franchini, Michele Reticcioli, Martin Setvin, and Ulrike Diebold. Polarons in materials. *Nature Reviews Materials*, 6(7):560–586, 2021.
- [70] Jiawei Lin, Kyu Jung Jun, and Gerbrand Ceder. Computational design of polaronic conductive Li-NASICON mixed ionic-electronic conductors. *Journal of Materials Chemistry A*, 2:15659–15672, 2025.
- [71] George V. Alexander, Changmin Shi, Jon O'Neill, and Eric D. Wachsman. Extreme lithium-metal cycling enabled by a mixed ion- and electron-conducting garnet three-dimensional architecture. *Nature Materials*, 22(9):1136–1143, 2023.
- [72] Thomas Scheiber, Bernhard Gadermaier, Matjaž Finšgar, and H. Martin R. Wilkening. Charge Carrier Dynamics of the Mixed Conducting Interphase in All-Solid-State Batteries: Lithiated Li1.3Al0.3Ti1.7(PO4)3 as a Case Study. *Advanced Functional Materials*, 7:1–14, 2024.
- [73] Qiongyu Zhou, Biyi Xu, Po Hsiu Chien, Yutao Li, Bing Huang, Nan Wu, Henghui Xu, Nicholas S. Grundish, Yan Yan Hu, and John B. Goodenough. NASICON Li1.2Mg0.1Zr1.9(PO4)3 Solid Electrolyte for an All-Solid-State Li-Metal Battery. Small Methods, 4(12):1-7, 2020.
- [74] Tara P Mishra, Zhuohan Li, Meghan Shen, Maximilian Jaugstetter, Livia P Matte, Jung O. Park, Hyunjin Kim, Benjamin X Lam, Karen Bustillo, Gerbrand Ceder, and Mary Scott. Investigating the Degradation of LATP Solid Electrolyte in High Alkaline Li-O₂ Batteries. page 1–33, 2025.
- [75] Eunryeol Lee, Dae-hyung Lee, Sang-wook Park, Dong-hwa Seo, and Jinhyuk Lee. Nearly all-active-material cathodes free of nickel and cobalt for Li-ion batteries. *Energy & Environmental Science*, 17:3753–3764, 2024.
- [76] K Arbi, M Hoelzel, A Kuhn, F Garc, and J Sanz. Structural Factors That Enhance Lithium Mobility in Fast-Ion Li 1+ conductors. *Inorg Chem*, 52(Figure 1):9290–9296, 2013.
- [77] Michele Catti, Angiolina Comotti, Silvia Di Blasa, and Richard M. Ibberson. Extensive lithium disorder in Li1.5Fe0.5Ti1.5(PO4)3 Nasicon by neutron diffraction, and the Li1+xFexTi2-x(PO4)3 phase diagram. *Journal of Materials Chemistry*, 14:835–539, 2004.
- [78] D. Morgan, G. Ceder, M. Y. Saïdi, J. Barker, J. Swoyer, H. Huang, and G. Adamson. Experimental and computational study of the structure and electrochemical properties of monoclinic LixM2(PO4)3 compounds. *Journal of Power Sources*, 119-121(10):755-759, 2003.
- [79] C. Delmas, A. Nadiri, and J. L. Soubeyroux. The nasicon-type titanium phosphates Ati2(PO4)3 (A=Li, Na) as electrode materials. Solid State Ionics, 28-30(PART 1):419-423, 1988.
- [80] Michael P O Callaghan, Andrew S Powell, Jeremy J Titman, George Z Chen, and Edmund J Cussen. Switching on Fast Lithium Ion Conductivity in Garnets: The Structure and Transport Properties of Li 3 + x Nd 3 Te 2 x Sb x O 12. *Chemistry of Materials*, 20:2360–2369, 2008.
- [81] Michael P O Callaghan, Andrew S Powell, Jeremy J Titman, George Z Chen, and Edmund J Cussen. Switching on Fast Lithium Ion Conductivity in Garnets: The Structure and Transport Properties of Li 3 + x Nd 3 Te 2 x Sb x O 12. *Chemistry of Materials*, 20:2360–2369, 2008.
- [82] Satoshi Hasegawa, Nobuyuki Imanishi, Tao Zhang, Jian Xie, Atsushi Hirano, Yasuo Takeda, and Osamu Yamamoto. Study on lithium/air secondary batteries-Stability of NASICON-type lithium ion conducting glass-ceramics with water. *Journal of Power Sources*, 189(1):371–377,

- 2009.
- [83] Sunny Wang, Edward Barks, Po Ting Lin, Xin Xu, Celeste Melamed, Geoff McConohy, Slavomír Nemsák, and William C. Chueh. Effect of H+ Exchange and Surface Impurities on Bulk and Interfacial Electrochemistry of Garnet Solid Electrolytes. *Chemistry of Materials*, 36:6849–6864, 2024.
- [84] Zhuohan Li, Benjamin X. Lam, and Gerbrand Ceder. Li+/H+ exchange in solid-state oxide Li-ion conductors. arXiv, page 1–33, 2025.
- [85] Zeyu Deng, Tara P Mishra, Eunike Mahayoni, Qianli Ma, Aaron Jue, Kang Tieu, Olivier Guillon, Jean-noël Chotard, Vincent Seznec, Anthony K Cheetham, Christian Masquelier, Gopalakrishnan Sai Gautam, and Pieremanuele Canepa. Fundamental investigations on the sodium- ion transport properties of mixed polyanion solid-state battery electrolytes. *Nature Communications*, 13:4470, 2022.
- [86] Jingyang Wang, Tanjin He, Xiaochen Yang, Zijian Cai, Yan Wang, Valentina Lacivita, Haegyeom Kim, Bin Ouyang, and Gerbrand Ceder. Design principles for NASICON super-ionic conductors. *Nature Communications*, 14(1), 2023.
- [87] S. V. Pershina, E. S. Kuznetsova, S. A. Belyakov, V. A. Elterman, R. K. Abdurakhimova, V. I. Voronin, and G. N. Starostin. Synthesis, structural investigations and properties of Si-modified Li1.5Al0.5Ge1.5(PO4)3 glass-ceramics. *Solid State Ionics*, 405(December 2023), 2024.
- [88] Asmaa Loutati, Olivier Guillon, Frank Tietz, and Dina Fattakhova-Rohlfing. NaSICON-type solid-state Li+ ion conductors with partial polyanionic substitution of phosphate with silicate. *Open Ceramics*, 12(November):100313, 2022.
- [89] Dohyeon Yu, Dan Na, Hwan Kim, Dong Ick Son, David D. Lee, and Inseok Seo. Si-substituted NASICON-type Li1.4Al0.4Ti1.6(PO4)3 solid electrolytes for enhanced stability and performance of Li-CO2 batteries. *Journal of Alloys and Compounds*, 1010(November 2024):177722, 2025.
- [90] Charles E Schwarz, Ramanuja Srinivasan Saravanan, Nina M Borodin, Yunsheng Liu, Eric D Wachsman, and Yifei Mo. Polaron-Based Electronic Conduction in Mixed Ionic-Electronic Conducting Lithium Garnets. ACS Energy Letters, 9:5334–5340, 2024.
- [91] Neelakshi Sharma and Anshuman Dalvi. Vanadium substituted Li+-NASICON systems: Tailoring electronic conductivity for electrode applications. *Journal of Alloys and Compounds*, 861:157954, 2021.
- [92] Shyue Ping Ong, William Davidson Richards, Anubhav Jain, Geoffroy Hautier, Michael Kocher, Shreyas Cholia, Dan Gunter, Vincent L. Chevrier, Kristin A. Persson, and Gerbrand Ceder. Python Materials Genomics (pymatgen): A robust, open-source python library for materials analysis. *Computational Materials Science*, 68:314–319, 2013.
- [93] G Kresse and D Joubert. From ultrasoft pseudopotentials to the projector augmented-wave method. *Phys. Rev. B*, 59(3):1758–1775, jan 1999.
- [94] G. Kresse and J. Furthmüller. Efficient iterative schemes for ab initio total-energy calculations using a plane-wave basis set. *Physical Review B Condensed Matter and Materials Physics*, 54(16):11169–11186, 1996.
- [95] John P. Perdew, Kieron Burke, and Matthias Ernzerhof. Generalized gradient approximation made simple. *Physical Review Letters*, 77(18):3865–3868, 1996.
- [96] Alexander Urban, Dong Hwa Seo, and Gerbrand Ceder. Computational understanding of Li-ion batteries. *npj Computational Materials*, 2(October 2015), 2016.

- [97] F. Zhou, M. Cococcioni, C. A. Marianetti, D. Morgan, and G. Ceder. First-principles prediction of redox potentials in transition-metal compounds with LDA + U. Physical Review B Condensed Matter and Materials Physics, 70(23):1–8, 2004.
- [98] Eric B. Isaacs, Shane Patel, and Chris Wolverton. Prediction of Li intercalation voltages in rechargeable battery cathode materials: Effects of exchange-correlation functional, van der Waals interactions, and Hubbard U. *Physical Review Materials*, 4(6):1–11, 2020.
- [99] Iurii Timrov, Francesco Aquilante, Matteo Cococcioni, and Nicola Marzari. Accurate Electronic Properties and Intercalation Voltages of Olivine-Type Li-Ion Cathode Materials from Extended Hubbard Functionals. *PRX Energy*, 1(3):1, 2022.
- [100] Lei Wang, Thomas Maxisch, and Gerbrand Ceder. Oxidation energies of transition metal oxides within the GGA + U framework. *Physical Reivew B*, (May):1–6, 2006.